

Article

Petrogenesis and Tectonic Implications of Late Carboniferous Intrusions in the Tuwu-Yandong Porphyry Cu Belt (NW China): Constraints from Geochronology, Geochemistry and Sr–Nd–Hf Isotopes

Weicai An ^{1,2}, Chunji Xue ^{1,*}, Yun Zhao ^{1,3,4} , Chao Li ^{2,*}, Dengfeng Xu ⁵ and Bo Chen ⁵

¹ State Key Laboratory of Geological Processes and Mineral Resources, China University of Geosciences, Beijing 100083, China

² National Research Center for Geoanalysis, Beijing 100037, China

³ Key Laboratory of Deep-Earth Dynamics of Ministry of Natural Resources, Institute of Geology, Chinese Academy of Geological Sciences, Beijing 100037, China

⁴ State Key Laboratory for Mineral Deposits Research, Nanjing University, Nanjing 210023, China

⁵ No. 2 Geological Surveying Institute, Xinjiang Bureau of Geology and Mineral Resources, Changji 831100, China

* Correspondence: chunji.xue@cugb.edu.cn (C.X.); re-os@163.com (C.L.)



Citation: An, W.; Xue, C.; Zhao, Y.; Li, C.; Xu, D.; Chen, B. Petrogenesis and Tectonic Implications of Late Carboniferous Intrusions in the Tuwu-Yandong Porphyry Cu Belt (NW China): Constraints from Geochronology, Geochemistry and Sr–Nd–Hf Isotopes. *Minerals* **2022**, *12*, 1573. <https://doi.org/10.3390/min12121573>

Academic Editor: Andrei Y. Barkov

Received: 1 November 2022

Accepted: 5 December 2022

Published: 7 December 2022

Publisher's Note: MDPI stays neutral with regard to jurisdictional claims in published maps and institutional affiliations.



Copyright: © 2022 by the authors. Licensee MDPI, Basel, Switzerland. This article is an open access article distributed under the terms and conditions of the Creative Commons Attribution (CC BY) license (<https://creativecommons.org/licenses/by/4.0/>).

Abstract: The Tuwu-Yandong porphyry Cu belt is located on the southern margin of the Dananhu island arc in eastern Tianshan, constituting the largest Cu metallogenic belt in Northwest China. Two episodes (~334 Ma and ~317 Ma) of porphyry Cu-Mo mineralization in the belt have been recognized, associated with Early and Late Carboniferous felsic intrusions, respectively. The Carboniferous intrusions, therefore, provide a unique opportunity to investigate tectono-magmatic-metallogenic evolution of the belt. New LA-ICP-MS zircon U-Pb dating indicates that the mineralization-related and post-mineralization intrusions (granodiorite porphyry, gabbro, and granite porphyry) were formed at 321.8 ± 3.1 Ma, 313.5 ± 1.2 Ma, and 309.8 ± 2.5 Ma, respectively. The zircon trace element shows that the granodiorite porphyry ($\text{Ce}^{4+}/\text{Ce}^{3+}$ ratios, avg. 129, median = 112, $n = 15$) was likely derived from a more oxidized (and hydrous) magma source than that of the gabbro ($\text{Ce}^{4+}/\text{Ce}^{3+}$ ratios, avg. 74, median = 40, $n = 15$) and granite porphyry ($\text{Ce}^{4+}/\text{Ce}^{3+}$ ratios, avg. 100, median = 91, $n = 15$), being favorable for porphyry copper mineralization. The granodiorite porphyry shows an adakitic affinity (e.g., high Sr/Y ratios and low Y contents) and has high $\varepsilon\text{Nd(t)}$ (6.4–6.7), $\varepsilon\text{Hf(t)}$ (11.4–14.3), and Mg[#] values (47.4–58.1) and low ($^{87}\text{Sr}/^{86}\text{Sr}$)_i (0.703804–0.703953), suggesting that the melt was derived from partial melting of a subducted oceanic slab followed by mantle peridotite interaction. The gabbro exhibits higher Al₂O₃ (16.5–17.4 wt. %), Cr (107–172 ppm), and Ni (37–77 ppm) contents and $\varepsilon\text{Nd(t)}$ (6.6–7.2), $\varepsilon\text{Hf(t)}$ (11.6–15.9), and Mg[#] (53.3–59.9) values, while it has lower ($^{87}\text{Sr}/^{86}\text{Sr}$)_i values (0.703681–0.703882) than the granodiorite porphyry, indicating a depleted mantle source. The granite porphyry exhibits an affinity with non-fractionated I-type granites and possesses higher SiO₂ (71.1–72.0 wt. %) contents, lower but positive $\varepsilon\text{Nd(t)}$ (4.8–5.2), $\varepsilon\text{Hf(t)}$ (10.3–13.0), and Mg[#] (38.7–41.0) values, and higher ($^{87}\text{Sr}/^{86}\text{Sr}$)_i (0.704544–0.704998) than the granodiorite porphyry and gabbro, together with young Nd and Hf model ages, suggesting that the parental magmas originated from the partial melting of a juvenile lower crust. The enrichment in LREEs and LILEs (e.g., Ba, U, K and Sr) and depletion in HFSEs (e.g., Nb, Ta, and Ti) indicate that these intrusive rocks formed in the subduction zone. With the integration of previous studies, it can be inferred that the northward flat subduction of the Kangguer ocean slab at ca. 335–315 Ma caused the formation of the adakites and associated porphyry Cu mineralization in the Tuwu-Yandong belt. After the prolonged flat subduction, slab rollback may have occurred at ca. 314–310 Ma, followed by a “quiet period” before the final closure of the ancient Tianshan Ocean along the Kangguer Fault in this belt.

Keywords: porphyry Cu deposits; petrogenesis; Tuwu-Yandong belt; eastern Tianshan

1. Introduction

The Central Asian Orogenic Belt (CAOB) was formed by the accretion of island arcs, ophiolites, oceanic islands, seamounts, accretionary wedges, oceanic plateau and microcontinents [1] and is one of the most important porphyry metallogenic domains worldwide [2]. A series of giant porphyry Cu–(Mo)–(Au) deposits that were formed from the Ordovician to the Jurassic, such as Kounrad, Aktogai, Kal’makyr, Oyu Tolgoi and Chalukou, which occurred in the Phanerozoic Central Asian Orogenic Belt (Figure 1a) [3]. The eastern Tianshan orogenic belt, located on the southern margin of the CAOB, consists of the Haerlike belt, the Jueluotage belt (including the Dananhu island arc, the Kangguer shear zone and the Yamansu arc) and the central Tianshan block (Figure 1b) [4] and constitutes an important Cu–Mo–Au–Ni–Fe–Ag metallogenic province in China [5,6]. Several porphyry Cu–(Mo)–(Au) deposits that are associated with Ordovician-Carboniferous intermediate to felsic porphyritic intrusions, have been discovered in the Dananhu island arc (Figure 1b), including the Yudai porphyry Cu–Au deposit [7], Sanchakou and Yuhai porphyry Cu–Mo deposit [8,9], and Tuwu-Yandong porphyry Cu–Mo–Au deposit [4,5]. The Tuwu-Yandong porphyry Cu belt, located on the southern margin of the Dananhu island arc, contains five Cu deposits (Figure 1b; Fuxing, Yandong, Tuwu, Linglong, and Chihu), with a proven Cu reserve of ca. 3 Mt [10]. These deposits, clustered in a ca. 15 km wide belt, show broad similarities in their mineralization and alteration styles, whereas they vary significantly in their ore reserves and copper grades [4,11–14]. Two episodes (335–330 Ma and 323–315 Ma) of porphyry Cu–Mo mineralization have been recognized in the Tuwu-Yandong belt [15–18], which are spatially and genetically related to Early and Late Carboniferous felsic intrusions (e.g., plagiogranite porphyry or tonalite porphyry, 339–332 Ma [5,10,19–21]; quartz albite porphyry, 323–319 Ma [10,13]; Chihu granodiorite and porphyritic granodiorite, 320–315 Ma [14]), respectively. Consequently, the Carboniferous intrusions provide an ideal subject for investigating the relationship between porphyry Cu metallogenesis and the tectonic background. Nevertheless, previous studies in the belt mainly focused on the Early Carboniferous intermediate–felsic intrusive rocks (e.g., diorite porphyry and diorite [5,10,19]; plagiogranite porphyry [5,10,19–23]; monzogranite [21]; quartz porphyry [5,10]), with little attention given to the Late Carboniferous mineralization-related and post-mineralization intrusions [10,13,14]. The tectonic setting of Late Carboniferous magmatism in this belt is still controversial, with the proposed models including a rift setting [24], a flat subduction- [25], slab-rollback- [10], or ridge-subduction-related island arc, and a post-collisional setting [26,27].

In this contribution, we present new zircon LA-ICP-MS U–Pb dating and trace element geochemistry, whole-rock geochemical data, and Sr–Nd isotope analyses, as well as *in situ* zircon Hf isotopic compositions of the Late Carboniferous intrusions (granodiorite porphyry, gabbro and granite porphyry), combined with the available data of the Carboniferous magmatic rocks, to better constrain the tectonic settings of the magmatism and mineralization of the Tuwu-Yandong porphyry copper metallogenic belt.

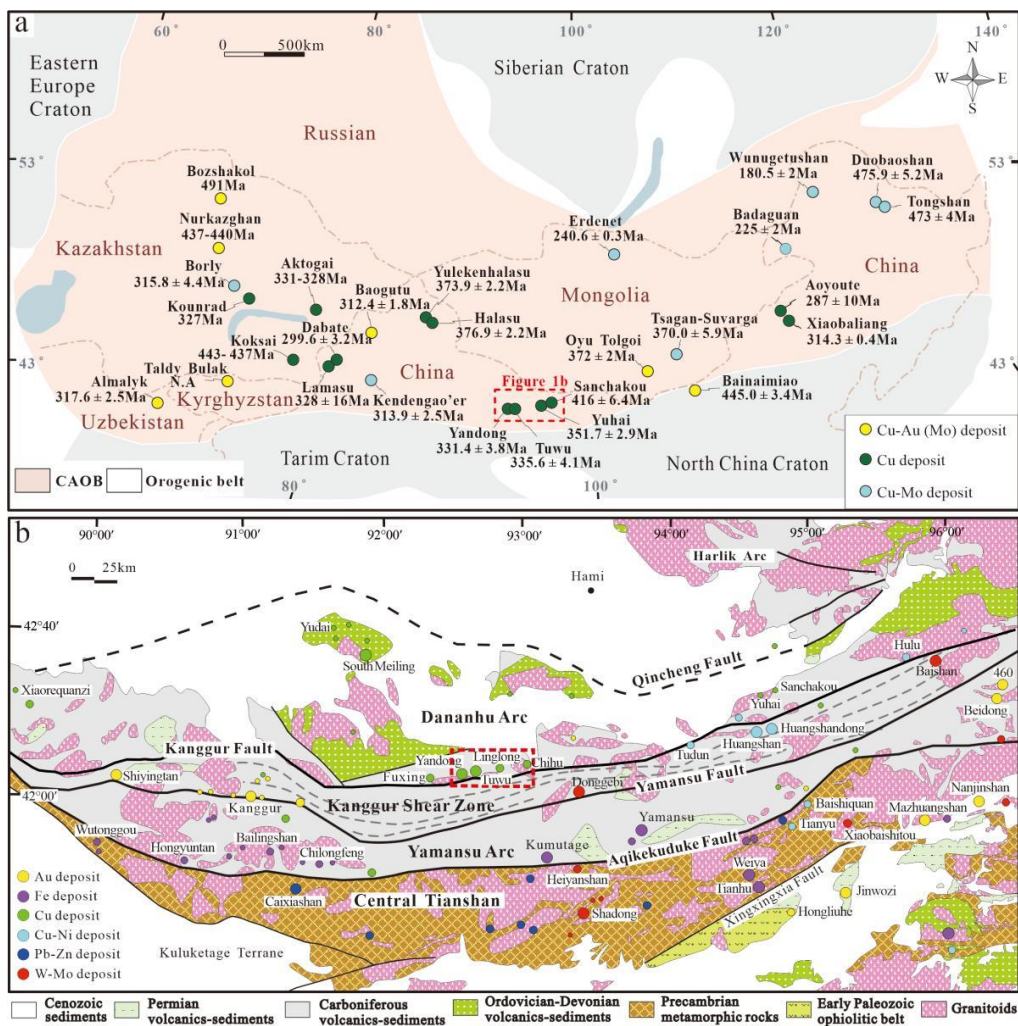


Figure 1. (a) Schematic map showing the distribution of major porphyry Cu–(Mo)–(Au) deposits in the Central Asian Orogenic Belt (CAOB; modified from [4]). (b) Tectonic framework and distribution of deposits in the eastern Tianshan (modified from [28]).

2. Geological Setting

The eastern Tianshan orogenic belt is a typical complex collage of island arc assemblages, remnants of oceanic crust, accretionary wedges, and continental fragments [29]. Generally, it may be divided from north to south into the Haerlike belt, Jueluotage belt, and central Tianshan block, separated by the regional-scale Qincheng and Aqikekuduke faults, respectively (Figure 1b) [4,8]. The Haerlike belt contains Ordovician-Carboniferous volcanic rocks, granites, and Late Paleozoic mafic-ultramafic complexes but only hosts a few porphyry Cu and Au prospects [4]. The central Tianshan block is composed mainly of a Precambrian crystalline basement and hosts several volcanic Fe deposits (e.g., Tianhu and Weiya) and the giant Caixiashan Pb–Zn deposit [30]. The Jueluotage belt is the most important Cu, Fe, and Au metallogenetic unit in eastern Tianshan [31] and can be further divided into three sub-tectonic domains by the Kanggur and Yamansu faults, namely the Dananhu island arc, the Kanggur shear zone, and the Yamansu arc (Figure 1b) [8]. The Dananhu island arc is characterized by Ordovician to Permian volcanic and clastic rocks and ultramafic to granitic intrusive rocks, as well as minor Jurassic coal-bearing clastic rocks [31], and hosts important porphyry Cu (e.g., Tuwu [4]) and volcanogenic massive sulfide Cu–Zn deposits (e.g., Honghai-Huangtupo [32]). The Kanggur shear zone mainly comprises dynamometamorphic Carboniferous-Permian marine volcanic-sedimentary rocks, including several ophiolite complexes and radiolarian bedded cherts, hosting ductile shear Au (e.g.,

Hongshi [33]), porphyry Mo (e.g., Donggebi [34,35]), and magmatic Cu-Ni sulfide deposits (e.g., Huangshannan [36]). The Yamansu arc consists of Carboniferous volcanic and volcanioclastic rocks with minor intercalated sedimentary rocks and Carboniferous to Permian intrusive rocks and hosts many Fe (e.g., Hongyuntan and Chilongfeng) and Fe–Cu (e.g., Bailingshan and Heijianshan) deposits [37].

The Tuwu-Yandong porphyry copper metallogenic belt is located on the southern margin of the Dananhu island arc between the Kangguer Fault and the Dacaotan Fault (Figure 2). Near-EW-, NW-, and NE-trending faults are widely developed in the area (Figure 2). The belt is mainly covered by the Carboniferous Qi’eshan Group, Jurassic Xishanyao Formation, and Quaternary sediments (Figure 2). The Qi’eshan Group consists of lower andesite and basalt lavas intercalated with tuff (CQ₁), middle andesite and brecciated andesite lavas (CQ₂), upper pebbly lithic sandstone, and minor tuffaceous siltstone intercalated with basalt, andesite, and dacite lavas (CQ₃) [4]. Previous studies indicate that the volcanic rocks of the Qi’eshan Group formed during the Early Carboniferous [10,19,20] based on the reported zircon U–Pb ages of the andesite (SHRIMP, 337 ± 7 Ma, [38]) and dacite (LA-ICP-MS, 344 ± 4 Ma, [39]). The porphyry Cu deposits/points mainly occur near the contact zone between the granitoid porphyries and the Qi’eshan Group (Figure 2). The Jurassic Xishanyao Formation, unconformably overlying the Qi’eshan Group, is mainly composed of sandstone, siltstone, mudstone, and conglomerate [4,10].

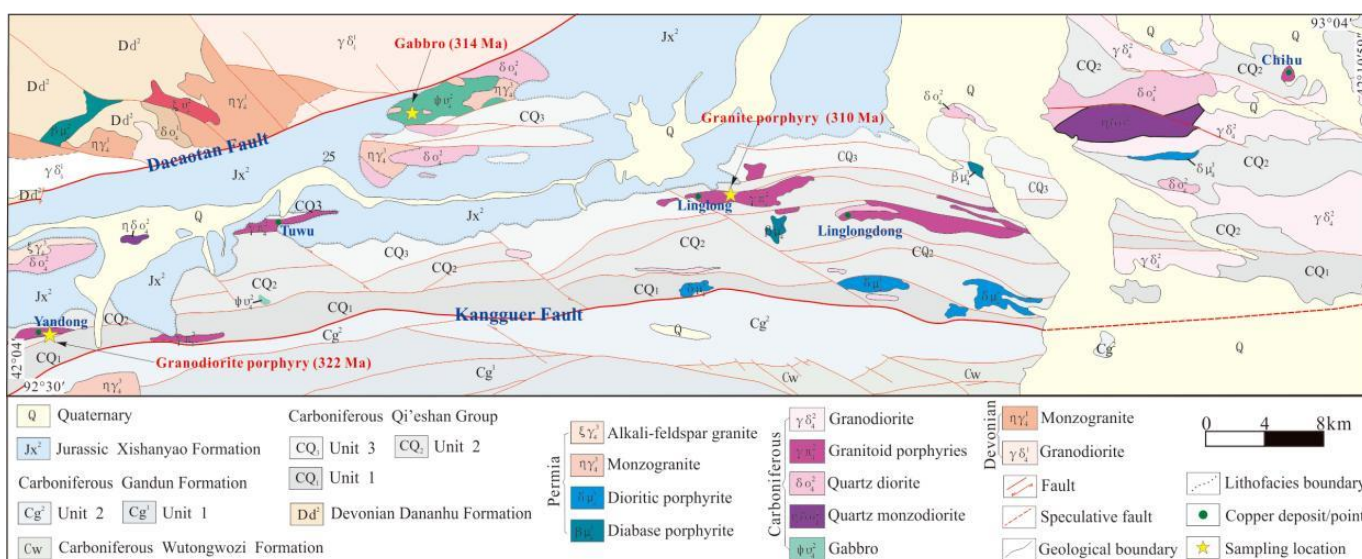


Figure 2. Regional geology and distribution of porphyry Cu deposits in the Tuwu-Yandong belt, eastern Tianshan (modified from unpublished map of geology, minerals, and comprehensive anomaly of the Tuwu-Chihu Belt, 2003, drawn by Xinjiang Institute of Geological Survey).

3. Sampling and Analytical Methods

3.1. Sampling

Large volumes of Carboniferous granitoid intrusions with minor mafic rocks (e.g., gabbro) are extensively distributed in the belt (Figure 2). One mafic intrusion (gabbro) and two felsic intrusions (granodiorite porphyry and granite porphyry) were selected for further geochronological and geochemical analyses. These intrusions are undeformed and lack recognizable post-magmatic alteration (Figure 3). The sampling locations are shown in Figure 2, and the mineral components are listed on Table 1. The studied granodiorite porphyry, gabbro, and granite porphyry intrude into the Qi’eshan Group (CQ₂ or CQ₃) in the Yandong, Tuwu, and Linglong areas, respectively (Figure 2). The granodiorite porphyry contains 20%–30% plagioclase, 5%–10% K-feldspar, and 15%–20% quartz, with minor biotite (Figure 3a–c). The gabbro consists of plagioclase (ca. 55%), pyroxene (ca. 35%), and

amphibole (ca. 10%) (Figure 3d,e). The granite porphyry is composed of plagioclase (ca. 20%), K-feldspar (ca. 10%), quartz (ca. 15%), and minor biotite (ca. 5%) (Figure 3g,h).

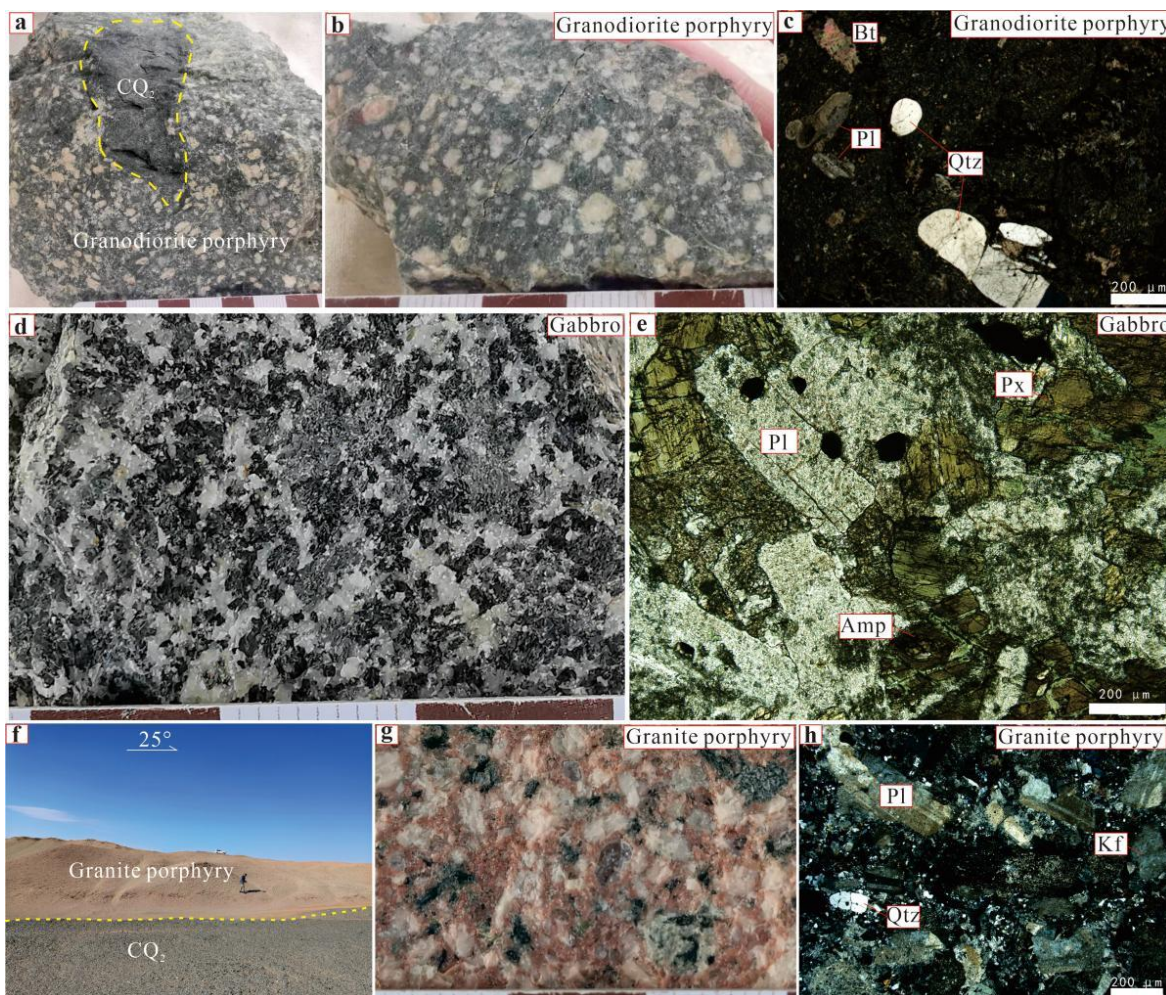


Figure 3. Field, hand specimen, and microscope photos of magmatic intrusions in the Tuwu-Yandong area. (a,b) Hand specimen of the granodiorite porphyry. (c) Photomicrograph of the granodiorite porphyry, showing plagioclase, quartz, and biotite phenocrysts under cross-polarized light. (d) Hand specimen of the gabbro. (e) The gabbro comprised of plagioclase, pyroxene, and amphibole under plane-polarized light. (f) The granite porphyry intruded into CQ₂. (g) Hand specimen of the granite porphyry. (h) Photomicrograph of the granite porphyry, showing plagioclase, K-feldspar, and quartz phenocrysts under cross-polarized light. Abbreviations: CQ₂, unit 2 of the Qi'eshan Group; Qtz, quartz; Pl, plagioclase; Bt, biotite; Px, pyroxene; Amp, amphibole; Kf, K-feldspar.

Table 1. Location and description of the studied intrusive rocks in the Tuwu-Yandong belt.

Rock Name	Sampling Location	Sampling Coordinate	Emplaced Strata	Texture	Major Mineral Components
Granodiorite porphyry	Yandong deposit	92°31'35" E, 42°05'27" N	CQ ₂	porphyritic	Phenocryst Pl (20%–30%) + Kf (5%–10%) + Qtz (15%–20%)
Gabbro	Northeast of Tuwu deposit	92°39'56" E, 42°09'25" N	CQ ₃	gabbro	Pl (55%) + Px (35%) + Amp (10%)
Granite porphyry	Linglong deposit	92°49'42" E, 42°07'58" N	CQ ₂	porphyritic	Phenocryst Pl (20%) + Kf (10%) + Qtz (15%) + Bt (5%)

Abbreviations: Qtz, quartz; Pl, plagioclase; Px, pyroxene; Amp, amphibole; Kf, K-feldspar; Bt, biotite.

3.2. Analytical Methods

The ten least altered samples were selected for whole-rock major and trace element as well as Sr–Nd isotopic analyses. Three samples were chosen for LA–ICP–MS zircon U–Pb isotopic dating, trace element geochemistry, and in situ Hf isotopic analyses.

The zircon grains were separated by routine physical elutriation, heavy liquid, and magnetic techniques and carefully hand-picked under a stereoscopic microscope. Subsequently, they were mounted on epoxy and polished to expose the crystal cross-sections. The documentation of the internal structures and selection of potential target sites for the U–Pb dating of all the mounted zircons were based on transmitted and reflected light photomicrographs, as well as cathodoluminescence (CL) images. Zircon U–Pb dating and trace element analyses were simultaneously conducted using an Agilent 7500 a inductively coupled plasma mass spectrometer (ICP–MS) coupled with a GeoLas 2005 at the Tianjin Institute of Geology and Mineral Resources. The analytical procedures were described by [40]. Laser ablation was operated at a constant energy of 60 mJ, with a repetition rate of 4 Hz and a spot diameter of 32 μm . NIST SRM 610 and zircons 91500, GJ-1, were used as external standards. Zircon 91500 was analyzed twice for every six analyses to calibrate the isotope fractionation. NIST SRM 610 was analyzed once every eight analyses to correct the instrumental drift and mass discrimination of the trace element analysis. Errors in individual analyses were cited at the 1σ level, and the weighted mean $^{206}\text{Pb}/^{238}\text{U}$ ages were quoted at the 95% confidence level. The adjustment of background and ablation signals, time drift correction, and quantitative calibration were performed using ICPMSDataCal software [40]. Concordia diagrams and weighted mean calculations were determined using Isoplot 3.71 [41]. Zircon Ce anomalies were calculated using the method based on the lattice strain model [42].

In situ Hf isotope analyses were undertaken on the adjacent spots used for the LA–ICP–MS zircon U–Pb dating in order to match the Hf isotope data with the U–Pb ages using a Neptune MC–ICP–MS and New Wave UP 213 ultraviolet LA–MC–ICP–MS at the National Research Center for Geoanalysis, Beijing, China. During the analyses, helium was used as the carrier gas. Based on the zircon size, the stationary beam spot size was set to either 55 or 40 μm . GJ1 international standard zircon samples were used as a reference. The weighted average of the $^{176}\text{Hf}/^{177}\text{Hf}$ of the GJ1 zircon samples was 0.282015 ± 31 (2 SD, $n = 10$), which is consistent with the values reported by [43]. Detailed operating conditions for the laser ablation system, the MC–ICP–MS instrument, and the analytical method are given by [44].

Whole-rock major and trace elements analyses were performed at the National Research Center for Geoanalysis, Beijing, China. The samples were chipped and powdered to approximately 200 mesh. The major elements were determined using a Philips PW 2404 X-ray fluorescence (XRF) spectrometer with a rhodium X-ray source. The testing precision was better than 1%. The sample powders for the trace element analyses were accurately weighed (25 mg) and placed into Savillex Teflon beakers within high-pressure bomb and were then digested using $\text{HF} + \text{HNO}_3 + \text{HClO}_4$ acid to ensure the complete dissolution of the refractory minerals. The trace elements, including rare earth elements, were determined using an Element-I plasma mass spectrometer (Finnigan-MAT Ltd. German), and the national geological standard reference samples GSR-3 and GSR-15 were used for the purpose of analytical quality control. The analytical precision for the trace elements was better than 5%, and the analytical procedures were described by [45].

Whole-rock Sr–Nd isotopic analyses were performed using a Micromass Isoprobe multi-collector ICP–MS at the National Research Center for Geoanalysis, Beijing, China, using analytical procedures described by [44]. The Sr and REE were separated using cation columns, and the Nd fractions were further separated using HDEHP-coated Kef columns. The measured $^{87}\text{Sr}/^{86}\text{Sr}$ and $^{143}\text{Nd}/^{144}\text{Nd}$ ratios were normalized to $^{86}\text{Sr}/^{88}\text{Sr} = 0.1194$ and $^{146}\text{Nd}/^{144}\text{Nd} = 0.7219$, respectively. The reported $^{87}\text{Sr}/^{86}\text{Sr}$ and $^{143}\text{Nd}/^{144}\text{Nd}$ ratios were, respectively, adjusted to the NBS SRM 987 standard $^{87}\text{Sr}/^{86}\text{Sr} = 0.71025$ and the Shin Etsu JNdi-1 standard $^{143}\text{Nd}/^{144}\text{Nd} = 0.512115$ [10].

4. Results

4.1. Whole-Rock Geochemistry

The whole-rock major and trace element contents are presented in Table 2. The granodiorite porphyry, gabbro, and granite porphyry samples are plotted within the fields of granodiorite, gabbro/monzo-diorite, and granite, respectively, in the total alkali–silica (TAS) diagram (Figure 4a) [46]. All these rocks belong to the calc-alkaline series (Figure 4b,c) and display low A/CNK ($\text{Al}_2\text{O}_3/(\text{CaO} + \text{Na}_2\text{O} + \text{K}_2\text{O})$, mole ratio) values (0.76–1.09, except for sample YD-55-4-95 at 1.24), indicating metaluminous to weakly peraluminous compositions (Figure 4d). All the intrusive samples are enriched in LREEs and LILEs (e.g., Ba, U, K and Sr) and depleted in HREEs and HFSEs (e.g., Nb, Ta and Ti) (Figure 5a,b).

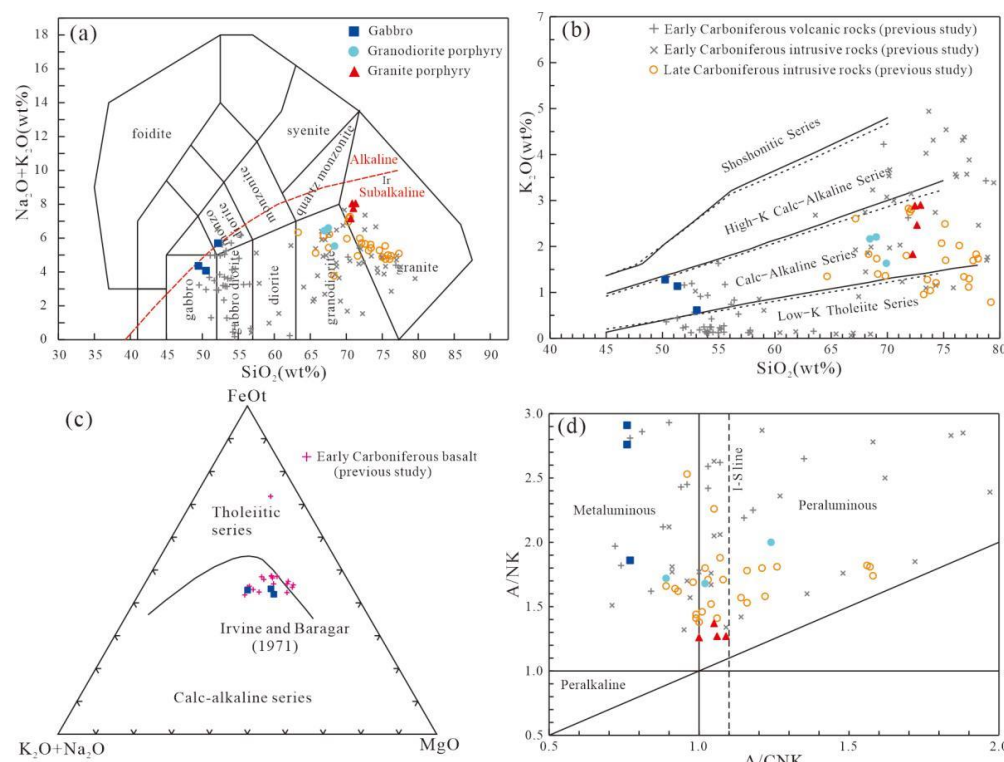


Figure 4. Classification and series diagrams of Late Carboniferous intrusions in the Tuwu-Yandong porphyry Cu Belt. (a) $\text{Na}_2\text{O} + \text{K}_2\text{O}$ vs. SiO_2 plot diagram [46]. (b) K_2O vs. SiO_2 diagram [47]. (c) AFM diagram ($A = \text{Na}_2\text{O} + \text{K}_2\text{O}$, $F = \text{FeOt}$, $M = \text{MgO}$). The boundary between the tholeiite and the calc-alkaline series is from [48]. (d) A/NK vs. A/CNK plot diagram [49]. The data from previous studies can be found in Supplementary Table S1.

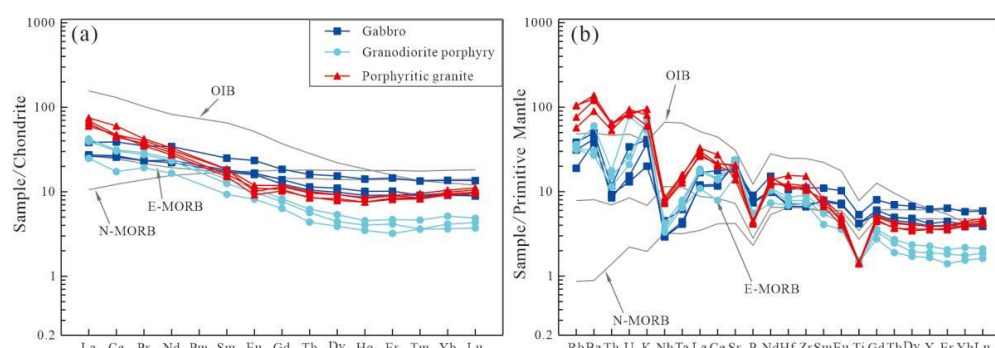


Figure 5. (a) Chondrite-normalized REE and (b) primitive mantle-normalized trace element abundance spider diagram of the Carboniferous intrusions in the Tuwu-Yandong porphyry Cu Belt (normalization values are from [50,51]). The N-MORB, E-MORB, and OIB patterns are from [51].

Table 2. Whole-rock geochemical data of the studied intrusive rocks in the Tuwu-Yandong belt (major elements: wt.%; trace elements: ppm).

Sample No.	YD-42	YD-46	YD-55-4-95	KBDB-5	KBDB-6	KBDB-7	LL-5	LL-6	LL-9	LL-10
Rock Type	GDP	GDP	GDP	GA	GA	GA	GP	GP	GP	GP
SiO ₂	66.81	65.94	67.86	52.02	50.37	49.08	71.11	71.53	71.96	71.39
TiO ₂	0.32	0.30	0.33	1.16	0.91	0.91	0.31	0.31	0.30	0.31
Al ₂ O ₃	15.60	15.52	15.87	16.46	17.38	17.40	14.54	14.16	14.53	14.56
Fe ₂ O ₃ ^T	3.01	2.79	2.59	9.74	9.10	9.30	2.58	2.42	2.26	2.34
MnO	0.06	0.06	0.15	0.19	0.15	0.15	0.24	0.08	0.05	0.06
MgO	1.54	1.27	1.81	5.62	6.31	7.00	0.87	0.85	0.72	0.82
CaO	3.26	4.56	2.66	6.93	9.22	9.04	1.76	1.58	1.04	1.25
Na ₂ O	4.25	4.12	3.79	4.99	2.89	3.01	5.25	5.22	5.08	5.08
K ₂ O	2.14	2.09	1.58	0.60	1.11	1.25	1.80	2.43	2.86	2.84
P ₂ O ₅	0.12	0.11	0.12	0.20	0.16	0.16	0.10	0.09	0.09	0.09
L.O.I	3.18	3.66	2.93	1.94	1.87	2.30	1.57	1.52	1.35	1.47
Total	100.28	100.41	99.69	99.85	99.48	99.60	100.14	100.18	100.24	100.21
Mg [#]	50.3	47.4	58.1	53.3	57.9	59.9	40.0	41.0	38.7	41.0
Sc	4.56	5.87	6.69	26.76	19.15	17.36	5.48	5.20	4.69	5.59
V	48.3	50.1	78.5	280.7	208.8	229.1	29.2	27.5	24.0	33.5
Cr	6.94	11.46	12.00	107.36	114.21	171.74	11.20	14.31	8.88	5.60
Co	11.79	12.64	12.31	43.63	41.21	49.72	9.27	9.26	7.30	8.26
Ni	8.44	10.75	14.14	36.47	72.19	77.04	4.391	4.73	1.56	3.06
Cu	22.68	20.54	37.22	27.46	69.61	69.39	21.47	12.27	9.92	12.33
Zn	43.39	45.59	223.50	157.40	93.88	124.70	1501.00	242.20	124.60	132.20
Ga	10.76	12.64	15.13	13.57	12.8	14.18	13.48	13.69	13.31	14.58
Ge	0.71	1.06	1.97	1.27	1.23	1.26	1.30	1.32	0.95	1.26
Rb	20.06	20.53	22.92	12.01	19.77	24.38	36.25	48.36	66.58	65.80
Sr	318	444	505	391	445	491	344	292	428	435
Y	7.57	8.60	10.34	28.22	17.85	18.98	16.25	17.70	16.15	17.85
Zr	80.1	87.5	101.6	124.6	79.7	74.1	127.1	116.5	131.3	170.7
Nb	2.37	2.53	3.02	3.23	2.08	2.11	5.18	5.62	5.29	6.07
Cs	1.84	1.84	2.56	0.38	0.53	0.60	0.67	0.74	1.30	1.38
Ba	188.1	212.2	418.8	265.0	294.1	346.8	625.7	839.5	877.3	962.0
La	7.70	12.24	13.08	11.89	8.46	8.16	20.00	23.23	18.56	21.46
Ce	13.99	24.54	25.25	31.44	21.58	20.74	35.90	48.45	38.12	38.17
Pr	2.35	3.35	3.54	4.26	2.84	2.84	4.56	5.16	4.27	4.90
Nd	9.94	13.95	14.72	20.56	13.29	14.18	17.43	19.79	16.38	18.55
Sm	1.81	2.44	2.75	4.88	3.37	3.51	3.14	3.61	2.96	3.61
Eu	0.60	0.72	0.81	1.72	1.18	1.22	0.81	0.88	0.67	0.74
Gd	1.64	1.98	2.14	4.77	3.20	3.60	2.76	3.06	2.65	2.97
Tb	0.21	0.27	0.29	0.75	0.49	0.54	0.40	0.47	0.41	0.45
Dy	1.26	1.43	1.73	4.95	3.18	3.55	2.67	2.99	2.54	2.97
Ho	0.25	0.29	0.33	1.01	0.65	0.73	0.54	0.60	0.54	0.62
Er	0.67	0.87	0.98	3.06	1.92	2.13	1.70	1.89	1.77	1.90
Tm	0.12	0.12	0.15	0.43	0.29	0.29	0.27	0.27	0.27	0.31
Yb	0.76	0.86	1.08	2.85	1.89	2.02	1.91	2.07	1.97	2.18
Lu	0.12	0.14	0.16	0.44	0.29	0.29	0.31	0.34	0.32	0.36
Hf	2.13	2.42	2.66	3.27	2.21	2.08	3.53	3.52	3.81	4.79
Ta	0.27	0.30	0.32	0.25	0.17	0.18	0.52	0.63	0.57	0.65
Pb	6.15	11.97	6.75	1.71	1.47	1.64	28.87	23.88	10.04	10.35
Th	0.97	1.28	1.50	0.79	0.72	0.99	4.52	5.37	5.33	5.50
U	0.44	0.55	1.64	0.27	0.32	0.71	1.82	1.97	1.71	1.78
Sr/Y	42.06	51.65	48.84	13.84	24.95	25.86	21.19	16.48	26.47	24.34
La/Yb _N	6.83	9.54	8.19	2.81	3.01	2.72	7.05	7.58	6.35	6.64
Dy/Yb _N	1.07	1.07	1.04	1.13	1.09	1.14	0.91	0.94	0.83	0.88
Th/La	0.13	0.10	0.11	0.07	0.08	0.12	0.23	0.23	0.29	0.26

Note: Mg [#] = 100 × (MgO/40.3044)/(MgO/40.3044 + 0.8998 × Fe₂O₃^T/71.8440). Abbreviation: GDP, granodiorite porphyry; GA, gabbro; GP, granite porphyry.

The granodiorite porphyry samples are characterized by relatively high SiO_2 (65.94–67.86 wt.%), Al_2O_3 (15.52–15.87 wt.%), Na_2O (3.79–4.25 wt.%), and $\text{Mg}^{\#}$ ($100 \times$ molar $\text{Mg}^{2+}/(\text{Mg}^{2+} + \text{Fe}^{2+})$) values (47.4–58.1), medium TiFe_2O_3 (2.59–3.01 wt.%), and low MgO (1.27–1.81 wt.%), K_2O (1.58–2.14 wt.%), TiO_2 (0.30–0.33 wt.%), MnO (0.06–0.15 wt.%), and P_2O_5 (0.11–0.12 wt%) contents. The granodiorite porphyry samples show more significant LREE/HREE differentiation ($[\text{La}/\text{Yb}]_{\text{N}} = 6.8$ –9.5) than the gabbro and granite porphyry, with slight positive or no Eu anomalies ($\text{Eu}/\text{Eu}^* = 0.98$ –1.04; Figure 5a). They possess low concentrations of Yb (0.76–1.08 ppm) and Y (7.57–10.34 ppm) and high Sr contents (318–505 ppm) and Sr/Y ratios (42–52), showing geochemical affinities with adakites [52]. In the Sr/Y versus Y diagrams (Figure 6a), they are plotted in the adakite field, overlapping with the field of Early Carboniferous ore-related adakites in the Tuwu-Yandong belt.

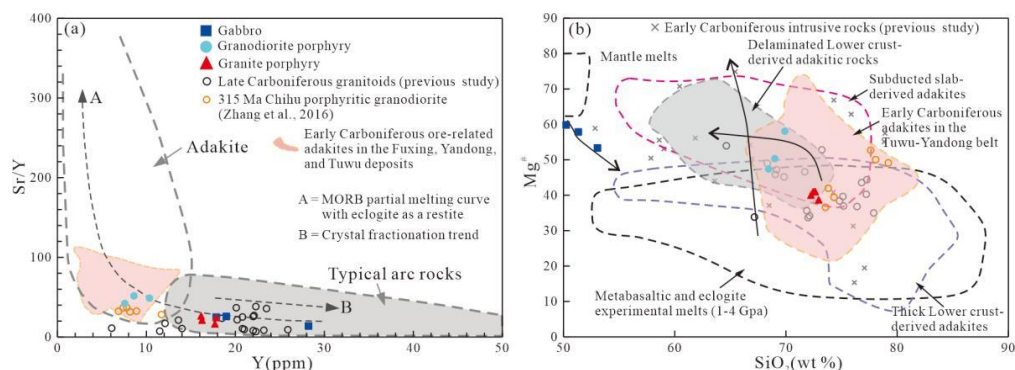


Figure 6. (a) Sr/Y vs. Y diagram (after [52]); (b) $\text{Mg}^{\#}$ vs. SiO_2 diagram (after [10]). The data from previous studies and the data on the Early Carboniferous ore-related adakites can be found in Supplementary Table S1.

The gabbro samples possess variable SiO_2 (49.08–52.02 wt.%), low TiO_2 (0.91–1.16 wt.%) contents, and intermediate MgO (5.62–7.00 wt.%) contents but higher Al_2O_3 (16.46–17.40 wt.%) contents and $\text{Mg}^{\#}$ values (53.3–59.9) than the granodiorite porphyry (Figure 6b), being geochemically similar to the high-Al basalt (HAB; $\text{SiO}_2 \leq 54$ wt.%, $\text{MgO} \leq 7$ wt.%, and $\text{Al}_2\text{O}_3 \geq 16.5$ wt.% [25]). The gabbro samples exhibit an Na-rich affinity, as suggested by high their Na_2O (2.89–4.99 wt.%) contents and $\text{Na}_2\text{O}/\text{K}_2\text{O}$ (2.4–8.3) values. They also have relatively high Cr (107.4–171.7 ppm), Ni (36.5–77.0 ppm), and Co (41.2–49.7 ppm) contents. Moreover, the gabbro samples show moderate LREE enrichment ($[\text{La}/\text{Yb}]_{\text{N}} = 2.7$ –3.0) and weak HREE fractionation ($[\text{Dy}/\text{Yb}]_{\text{N}} = 1.1$), with slight positive Eu anomalies ($\text{Eu}/\text{Eu}^* = 1.04$ –1.08; Figure 5a).

The granite porphyry samples are geochemically different from the granodiorite porphyry and gabbro samples. They possess higher SiO_2 (71.11–71.96 wt.%) and Na_2O (5.08–5.25 wt.%) and lower MgO (0.72–0.87 wt.%), TiFe_2O_3 (2.26–2.58 wt.%), and CaO (1.04–1.76 wt.%) contents and $\text{Mg}^{\#}$ values (38.7–41.0). They also have low Cr (5.6–14.3 ppm), Ni (1.6–4.7 ppm), and Co (7.3–9.3 ppm) contents, as well as low Nb/Ta (8.9–9.9), but relatively high Zr/Sm (32.2–47.3) ratios, displaying concave-upward REE patterns ($[\text{La}/\text{Yb}]_{\text{N}} = 6.4$ –7.6, $[\text{Dy}/\text{Yb}]_{\text{N}} = 0.83$ –0.94) with pronounced negative Eu anomalies ($\text{Eu}/\text{Eu}^* = 0.67$ –0.78; Figure 5a).

4.2. Zircon U-Pb Dating and Trace Element Geochemistry

All the analyzed zircons are colorless, euhedral, and prismatic, with an aspect ratio of 2:1 to 4:1. Most of them show typical magmatic oscillatory zoning in the CL images (Figure 7). The zircon LA-ICP-MS U-Pb dating data are listed in Table 3 and graphically illustrated in Figure 8a–c, and the zircon trace element data are summarized in Table 4. The Th/U ratios of the analyzed zircons range from 0.16 to 1.4 (Figure 8d), which are higher than those of the metamorphic zircons (typically <0.1) but consistent with those of magmatic zircons [53]. The REE patterns of the analyzed zircons are characterized by

HREE enrichment with positive Ce and negative Eu anomalies (Figure 9), consistent with those of magmatic zircon from igneous rocks [53,54]. Therefore, the zircon U–Pb dating results are interpreted to provide the age of magma crystallization.

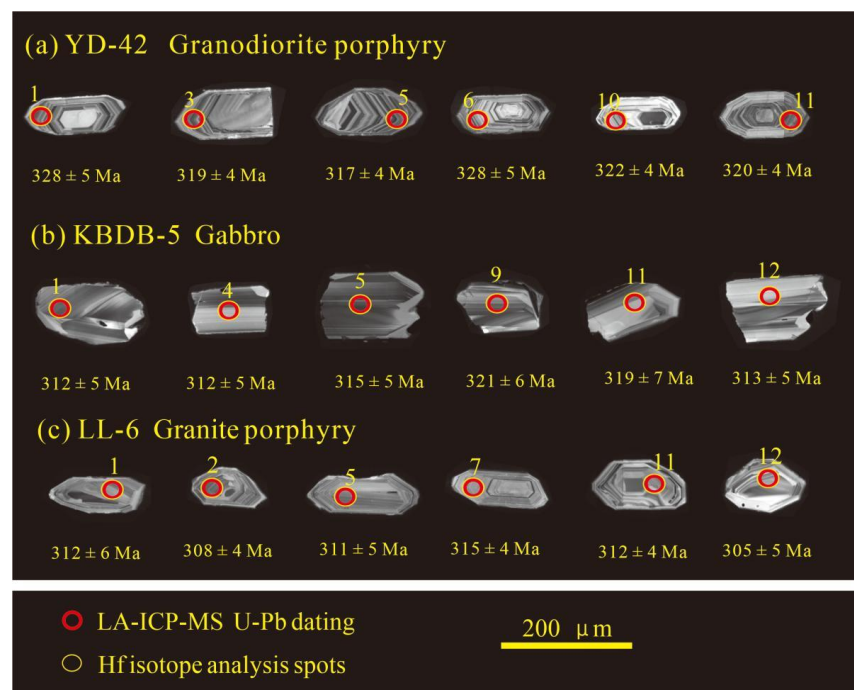


Figure 7. Cathodoluminescence images of representative zircon grains showing the inner structures and analyzed locations.

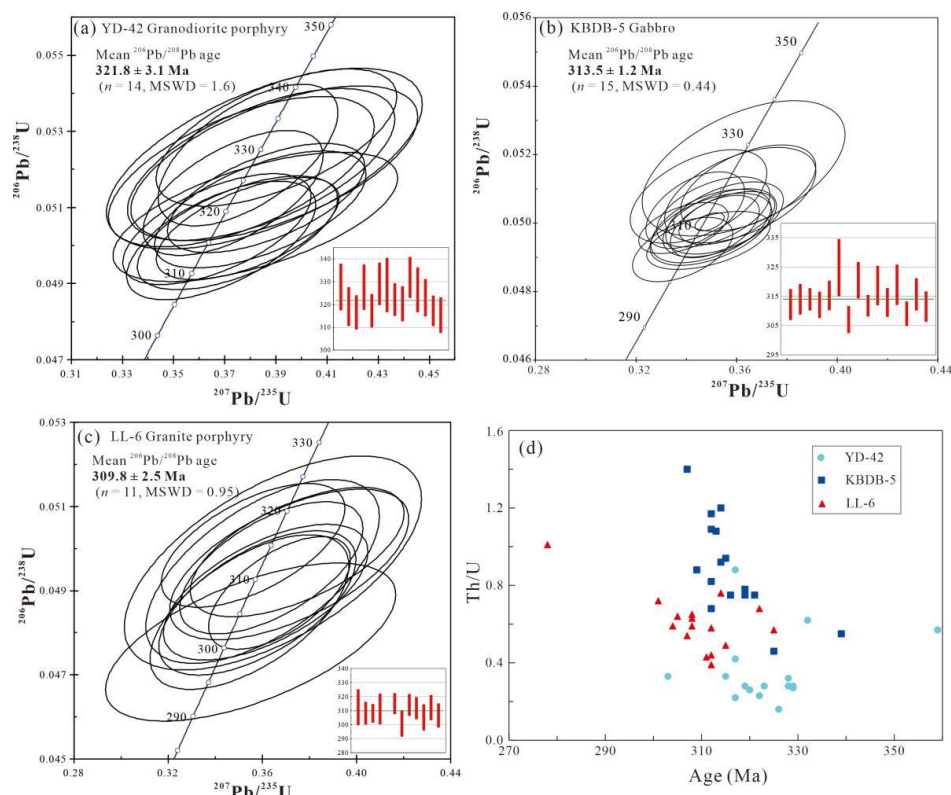


Figure 8. (a–c) $206\text{Pb}/238\text{U}$ vs. $207\text{Pb}/235\text{U}$ concordia diagrams and (d) Th/U vs. age diagram of zircons for the intrusive rocks.

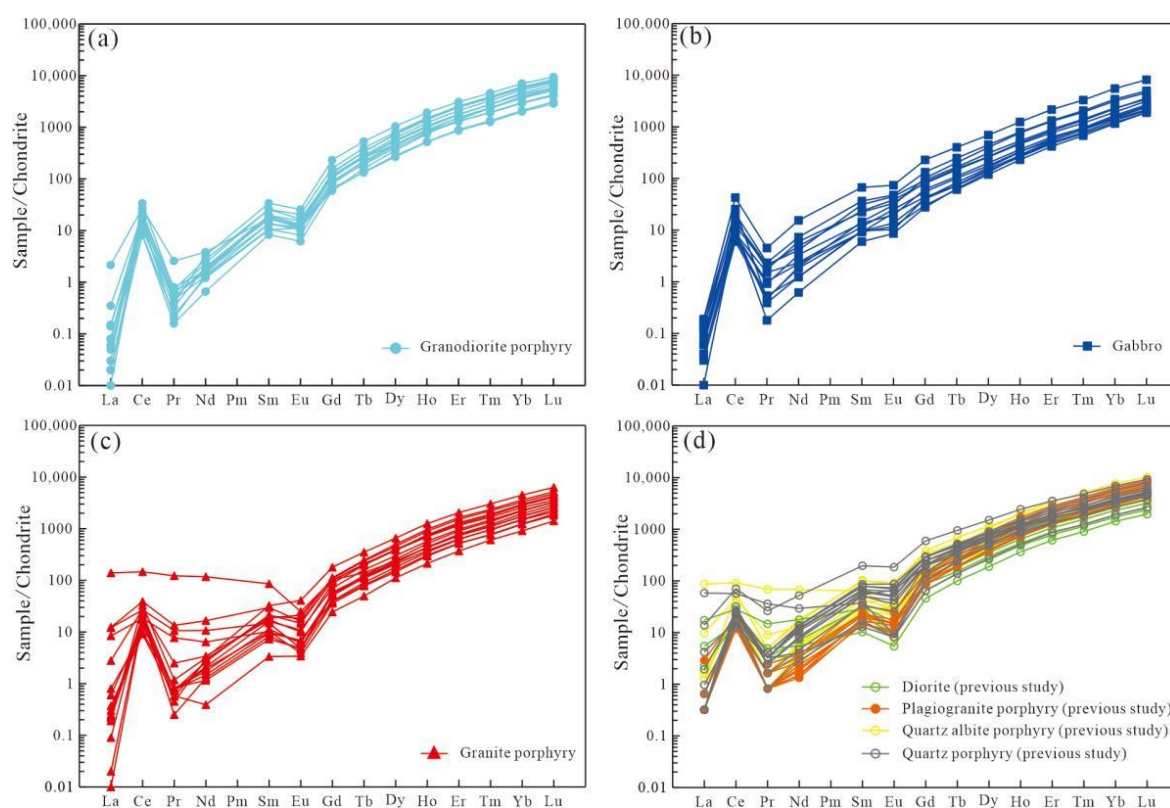


Figure 9. Chondrite-normalized REE patterns for the zircons from the granodiorite porphyry (a), gabbro (b), granite porphyry (c), and previously studied intrusive rocks (d) in the Tuwu-Yandong belt. The chondrite values are from [51]. The data for the diorite, plagiogranite porphyry, quartz albite porphyry, and quartz porphyry of the Tuwu-Yandong deposits are from [10].

Sixteen zircon grains from the granodiorite porphyry (YD-42) were analyzed and, excluding two discordant analyses (No. 02 and 04), the remaining fourteen data yielded $^{206}\text{Pb}/^{238}\text{U}$ ages ranging from 315 to 332 Ma, which form a coherent group and give a weighted mean age of 321.8 ± 3.1 Ma (MSWD = 1.6) (Figure 8a). The younger age (303 Ma) of analysis No. 02 is probably attributed to the effect of post-magmatic hydrothermal events, and the older age (359 Ma) of analysis No. 04 may indicate that the zircon grain is inherited. Among the sixteen analyses of the zircon grains from the gabbro (KBDB-5), fifteen concordant analyses yielded $^{206}\text{Pb}/^{238}\text{U}$ ages of 307–325 Ma, with a weighted mean age of 313.5 ± 1.2 Ma (MSWD = 0.54) (Figure 8b). One discordant analysis (No. 10) yielded an apparent $^{206}\text{Pb}/^{238}\text{U}$ age of 339 ± 7 Ma, which was interpreted as the age of the inherited zircon. Three of the sixteen zircon grains analyzed from the granite porphyry (LL-6) were discordant (No. 10, 13 and 15), possibly suggesting partial Pb loss. Zircon grain No. 03 and 06 yielded $^{206}\text{Pb}/^{238}\text{U}$ ages of 322 ± 5 Ma and 325 ± 5 Ma, respectively, which are similar to the previously determined U–Pb age of quartz albite porphyry (318.6 ± 3.0 Ma, [13]). The other eleven analyses fell on the concordia and yielded $^{206}\text{Pb}/^{238}\text{U}$ ages of 301 to 315 Ma, with a weighted mean age of 309.8 ± 2.5 Ma (MSWD = 0.82) (Figure 8c).

Ti-in-zircon thermometer and zircon $\text{Ce}^{4+}/\text{Ce}^{3+}$ ratios are used to estimate the temperatures and oxidation states of silicate magmas [42,55]. The calculated Ti-in-zircon temperatures range from 642 to 763 °C (avg. 688 °C, median = 673 °C, $n = 15$) in the granodiorite porphyry, 697 to 825 °C (avg. 742 °C, median = 740 °C, $n = 15$) in the gabbro, and 665 to 813 °C (avg. 728 °C, median = 711 °C, $n = 15$) in the granite porphyry (Table 4). The zircon $\text{Ce}^{4+}/\text{Ce}^{3+}$ ratios of the granodiorite porphyry, gabbro, and granite porphyry vary from 55 to 254 (avg. 129, median = 112, $n = 15$), 23 to 229 (avg. 74, median = 40, $n = 15$) and 29 to 308 (avg. 100, median = 91, $n = 15$), respectively (Table 4).

4.3. Zircon Hf Isotopes

The zircon Hf isotopic compositions are listed in Table 5 and shown in Figure 10a,b. The granodiorite porphyry, gabbro, and granite porphyry yielded $\varepsilon_{\text{Hf}}(t)$ values of 11.4–14.3, 11.6–15.9, and 10.3–13.0, respectively. The zircon Hf single- and two-stage model ages ($T_{\text{DM}1}$ and $T_{\text{DM}2}$) are 385–504 Ma and 418–603 Ma for the granodiorite porphyry, 310–493 Ma and 310–591 Ma for the gabbro, and 429–540 Ma and 494–663 Ma for the granite porphyry (Table 5).

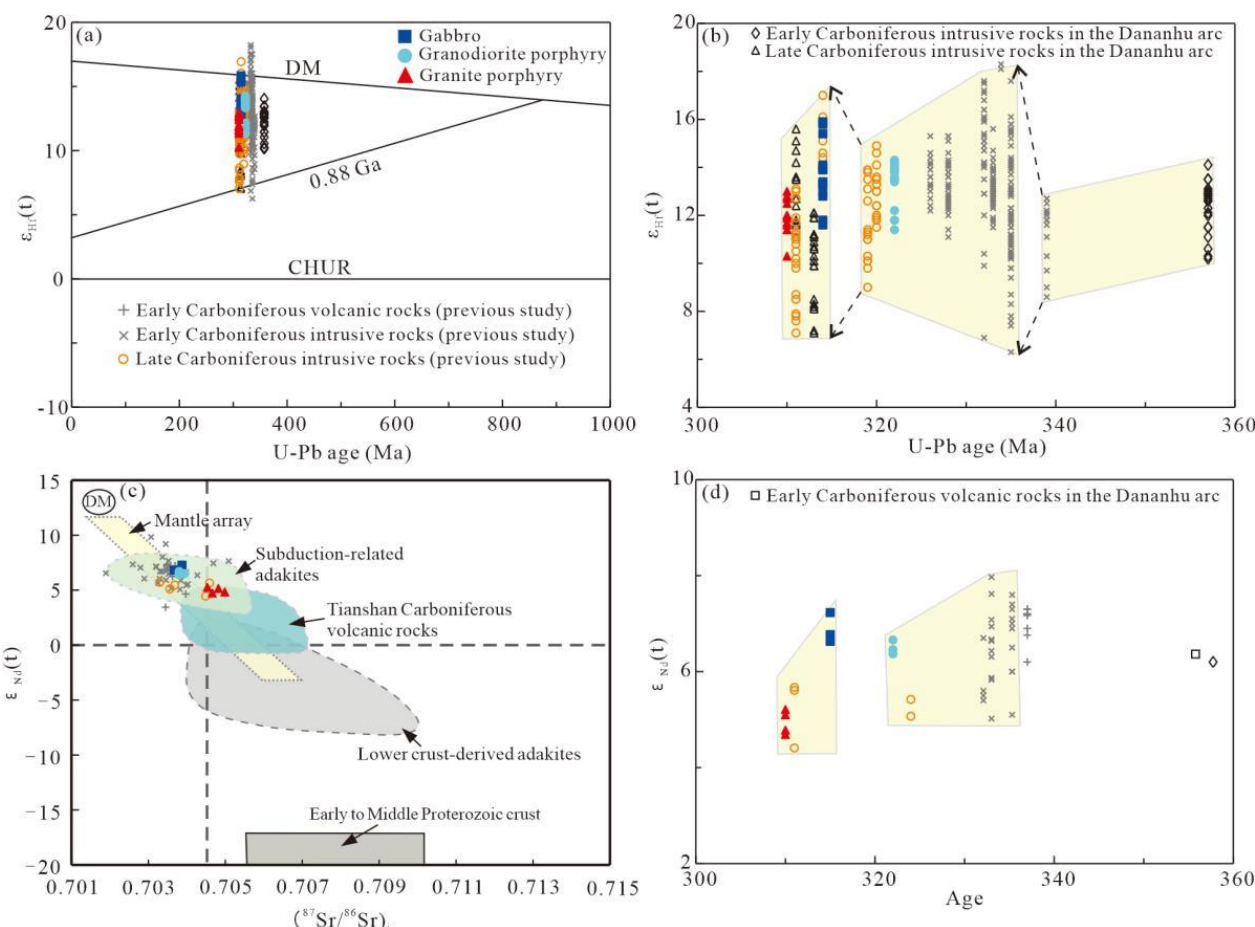


Figure 10. (a,b) $\varepsilon_{\text{Hf}}(t)$ vs. age (Ma) diagrams, (c) $\varepsilon_{\text{Nd}}(t)$ vs. $(^{87}\text{Sr}/^{86}\text{Sr})_i$ diagram (after [5]), and (d) $\varepsilon_{\text{Nd}}(t)$ vs. age (Ma) diagram for the magmatic rocks from the Tuwu-Yandong belt (and adjacent areas in the middle section of the Dananhu island arc). The data from previous studies can be found in Supplementary Tables S2 and S3.

4.4. Whole-Rock Sr–Nd Isotopic Compositions

The whole-rock Rb–Sr and Sm–Nd isotope compositions are summarized in Table 6 and shown in Figure 10c,d. The initial $^{87}\text{Sr}/^{86}\text{Sr}$ ratios and $\varepsilon_{\text{Nd}}(t)$ values were calculated based on the zircon U–Pb ages. All the samples display a relatively limited $(^{87}\text{Sr}/^{86}\text{Sr})_i$ variation and positive $\varepsilon_{\text{Nd}}(t)$ values (Figure 10c). The $(^{87}\text{Sr}/^{86}\text{Sr})_i$, $\varepsilon_{\text{Nd}}(t)$, and T_{DM} are 0.703804–0.703953, 6.37–6.66, and 528–545 Ma for the granodiorite porphyry, 0.703681–0.703882, 6.63–7.23, and 549–646 Ma for the gabbro, and 0.704544–0.704998, 4.78–5.21, and 619–688 Ma for the granite porphyry (Table 6). Among these intrusive rocks, the gabbro has the highest $\varepsilon_{\text{Nd}}(t)$ values, and the granite porphyry has the lowest $\varepsilon_{\text{Nd}}(t)$ values (Figure 10d) but the oldest T_{DM} .

Table 3. LA–ICP–MS zircon U–Pb data for the studied intrusive rocks in the Tuwu–Yandong belt.

No.	Concentrations and Ratios				Isotope Ratios						Ages (Ma)					
	Pb (ppm)	Th (ppm)	U (ppm)	Th/U	207Pb/206Pb	1σ	207Pb/235U	1σ	206Pb/238U	1σ	207Pb/206Pb	1σ	207Pb/235U	1σ	206Pb/238U	1σ
Granodiorite porphyry (Sample YD-42)																
YD-42.01	14	73	229	0.32	0.0541	0.0033	0.3894	0.0229	0.0522	0.0008	377	136	334	17	328	5
YD-42.02	13	75	226	0.33	0.0534	0.0022	0.3556	0.0148	0.0481	0.0006	345	93	309	11	303	4
YD-42.03	9	41	144	0.28	0.0545	0.0032	0.3820	0.0227	0.0508	0.0007	390	134	328	17	319	4
YD-42.04	8	55	95	0.57	0.0920	0.0044	0.7205	0.0337	0.0574	0.0010	1468	92	551	20	359	6
YD-42.05	14	53	241	0.22	0.0540	0.0025	0.3750	0.0160	0.0503	0.0006	372	105	323	12	317	4
YD-42.06	7	29	104	0.28	0.0544	0.0032	0.3843	0.0213	0.0521	0.0008	387	131	330	16	328	5
YD-42.07	13	167	189	0.88	0.0531	0.0022	0.3670	0.0150	0.0504	0.0006	333	96	317	11	317	4
YD-42.08	13	57	209	0.27	0.0521	0.0023	0.3791	0.0143	0.0524	0.0008	290	100	326	11	329	5
YD-42.09	5	24	84	0.28	0.0547	0.0041	0.3855	0.0252	0.0523	0.0010	402	170	331	18	329	6
YD-42.10	17	64	283	0.23	0.0549	0.0024	0.3862	0.0157	0.0512	0.0006	410	97	332	12	322	4
YD-42.11	13	55	208	0.26	0.0546	0.0028	0.3839	0.0169	0.0509	0.0006	397	117	330	12	320	4
YD-42.12	11	100	161	0.62	0.0536	0.0026	0.3902	0.0192	0.0528	0.0007	356	110	335	14	332	5
YD-42.13	8	23	138	0.16	0.0525	0.0030	0.3765	0.0212	0.0519	0.0008	309	132	324	16	326	5
YD-42.14	14	63	224	0.28	0.0525	0.0019	0.3733	0.0144	0.0514	0.0007	308	83	322	11	323	4
YD-42.15	20	131	308	0.42	0.0545	0.0023	0.3790	0.0146	0.0504	0.0005	393	94	326	11	317	3
YD-42.16	16	88	262	0.33	0.0535	0.0023	0.3686	0.0151	0.0501	0.0006	351	95	319	11	315	4
Gabbro (Sample KBDB-5)																
KBDB-5.01	9	110	133	0.82	0.0533	0.0036	0.3649	0.0205	0.0496	0.0009	342	152	316	15	312	5
KBDB-5.02	14	185	201	0.92	0.0540	0.0030	0.3720	0.0201	0.0499	0.0008	373	124	321	15	314	5
KBDB-5.03	23	370	307	1.20	0.0542	0.0025	0.3732	0.0164	0.0499	0.0006	380	105	322	12	314	4
KBDB-5.04	17	246	225	1.09	0.0536	0.0024	0.3670	0.0152	0.0496	0.0007	356	101	317	11	312	5
KBDB-5.05	12	157	166	0.94	0.0530	0.0032	0.3662	0.0193	0.0501	0.0008	328	136	317	14	315	5
KBDB-5.06	2	16	35	0.46	0.0573	0.0066	0.3818	0.0346	0.0517	0.0016	502	256	328	25	325	10
KBDB-5.07	21	413	296	1.40	0.0520	0.0026	0.3503	0.0171	0.0488	0.0008	283	115	305	13	307	5
KBDB-5.08	8	82	108	0.75	0.0546	0.0032	0.3842	0.0230	0.0510	0.0010	398	133	330	17	321	6
KBDB-5.09	20	324	276	1.17	0.0511	0.0023	0.3507	0.0153	0.0496	0.0006	243	71	305	11	312	4
KBDB-5.10	5	39	72	0.55	0.0527	0.0041	0.3838	0.0236	0.0540	0.0011	322	176	330	17	339	7
KBDB-5.11	5	59	76	0.78	0.0513	0.0036	0.3585	0.0233	0.0507	0.0011	254	161	311	17	319	7
KBDB-5.12	12	181	168	1.08	0.0539	0.0033	0.3695	0.0194	0.0497	0.0008	365	137	319	14	313	5
KBDB-5.13	5	56	75	0.75	0.0543	0.0040	0.3801	0.0258	0.0507	0.0011	385	164	327	19	319	7
KBDB-5.14	7	95	107	0.88	0.0532	0.0032	0.3636	0.0211	0.0491	0.0007	345	135	315	16	309	4

Table 3. *Cont.*

No.	Concentrations and Ratios				Isotope Ratios						Ages (Ma)					
	Pb (ppm)	Th (ppm)	U (ppm)	Th/U	207Pb/206Pb	1σ	207Pb/235U	1σ	206Pb/238U	1σ	207Pb/206Pb	1σ	207Pb/235U	1σ	206Pb/238U	1σ
KBDB-5.15	11	124	165	0.75	0.0519	0.0025	0.3568	0.0168	0.0502	0.0009	280	113	310	13	316	6
KBDB-5.16	7	69	103	0.68	0.0534	0.0033	0.3649	0.0208	0.0495	0.0008	348	140	316	15	312	5
Granite porphyry (Sample LL-6)																
LL-6.01	5	37	85	0.44	0.0566	0.0051	0.3645	0.0258	0.0497	0.0010	475	198	316	19	312	6
LL-6.02	11	109	174	0.63	0.0542	0.0031	0.3614	0.0177	0.0490	0.0007	378	130	313	13	308	4
LL-6.03	23	212	310	0.68	0.0791	0.0043	0.5745	0.0375	0.0513	0.0009	1174	107	461	24	322	5
LL-6.04	15	139	237	0.59	0.0542	0.0022	0.3673	0.0123	0.0489	0.0005	379	90	318	9	308	3
LL-6.05	9	62	144	0.43	0.0528	0.0034	0.3601	0.0202	0.0495	0.0009	321	147	312	15	311	5
LL-6.06	12	103	180	0.57	0.0532	0.0033	0.3872	0.0193	0.0518	0.0008	336	140	332	14	325	5
LL-6.07	11	86	178	0.49	0.0514	0.0026	0.3560	0.0159	0.0501	0.0006	260	115	309	12	315	4
LL-6.08	8	84	116	0.72	0.0539	0.0044	0.3550	0.0252	0.0478	0.0008	366	185	308	18	301	5
LL-6.09	16	179	235	0.76	0.0544	0.0028	0.3747	0.0185	0.0499	0.0006	389	115	323	14	314	4
LL-6.10	14	130	200	0.65	0.0781	0.0065	0.5533	0.0536	0.0489	0.0008	1149	166	447	35	308	5
LL-6.11	10	90	156	0.58	0.0533	0.0024	0.3638	0.0159	0.0495	0.0006	340	102	315	12	312	4
LL-6.12	10	99	154	0.64	0.0532	0.0028	0.3545	0.0172	0.0485	0.0008	337	120	308	13	305	5
LL-6.13	18	293	289	1.01	0.0521	0.0029	0.3198	0.0185	0.0441	0.0008	290	128	282	14	278	5
LL-6.14	5	34	88	0.39	0.0544	0.0035	0.3714	0.0207	0.0496	0.0007	390	143	321	15	312	4
LL-6.15	10	92	157	0.59	0.0743	0.0058	0.5048	0.0404	0.0482	0.0007	1051	156	415	27	304	4
LL-6.16	8	73	134	0.54	0.0527	0.0025	0.3579	0.0171	0.0487	0.0007	316	110	311	13	307	4

Table 4. Trace element abundance (in ppm), Eu anomalies, and $\text{Ce}^{4+}/\text{Ce}^{3+}$ in zircon and Ti-in-zircon temperature.

Analysis	Ti	La	Ce	Pr	Nd	Sm	Eu	Gd	Tb	Dy	Ho	Er	Tm	Yb	Lu	δEu^1	$\text{Ce}^{4+}/\text{Ce}^{3+}^2$	T (°C)3	$\log f\text{O}_2$ 4	Age (Ma)
Granodiorite porphyry (sample YD-42)																				
YD-42.01	7.18	0.110	16.2	0.080	0.89	3.87	1.13	28.3	12.4	172	72.4	366	90.0	965	214	0.37	152	763	-8.4	328
YD-42.02	2.26	0.026	13.2	0.061	1.15	3.23	0.93	27.4	12.4	181	76.8	376	89.5	903	189	0.30	107	662	-15.1	303
YD-42.03	3.06	0.006	12.5	0.025	0.81	2.65	0.77	22.9	10.4	150	64.1	323	75.4	765	166	0.31	142	686	-12.7	319
YD-42.05	2.49	0.045	9.3	0.041	1.18	3.80	0.97	34.7	15.8	233	101	509	119	1203	258	0.26	76	669	-16.0	317
YD-42.06	2.60	0.000	9.6	0.019	0.41	1.43	0.38	13.2	5.69	84.1	39.3	204	51.5	547	126	0.28	254	673	-11.2	328
YD-42.07	3.46	0.010	27.2	0.088	1.66	5.00	1.23	30.6	12.1	151	60.2	278	61.9	611	132	0.34	100	697	-13.4	317
YD-42.08	2.53	0.000	13.6	0.029	0.80	3.19	0.75	25.5	11.5	171	77.2	407	100	1064	237	0.27	172	671	-12.8	329
YD-42.09	5.21	0.017	7.0	0.028	0.73	2.02	0.82	15.8	6.42	91.2	38.0	188	43.5	438	101	0.46	81	733	-12.2	329
YD-42.10	2.53	0.043	15.6	0.098	1.00	3.82	0.93	33.6	15.5	240	106	538	127	1266	272	0.26	152	671	-13.3	322
YD-42.11	2.51	0.023	9.1	0.056	0.78	2.08	0.60	20.7	9.56	142	62.2	324	77.7	789	174	0.27	128	670	-14.0	320
YD-42.12	4.13	0.670	21.9	0.320	2.31	3.34	0.83	23.0	8.94	128	56.4	271	63.1	628	138	0.25	89	712	-13.0	332
YD-42.13	1.76	0.007	6.7	0.019	0.40	1.62	0.46	15.3	7.48	115	53.3	295	75.9	822	190	0.29	212	642	-13.8	326
YD-42.14	2.28	0.016	12.1	0.064	1.04	3.57	0.85	30.3	13.2	200	88.1	442	106	1092	236	0.26	112	662	-15.0	323
YD-42.15	3.30	0.004	18.5	0.074	1.42	5.02	1.51	41.7	18.6	259	109	518	120	1183	248	0.34	104	693	-13.5	317
YD-42.16	4.13	0.004	14.4	0.049	1.97	6.58	1.88	60.1	25.0	336	138	652	149	1471	303	0.32	55	712	-14.8	315
Gabbro (Sample KBDB-5)																				
KBDB-5.01	4.39	0.031	7.1	0.180	1.41	2.27	1.85	14.3	4.76	57.1	23.9	115	28.6	301	68.8	0.97	38	717	-15.9	312
KBDB-5.02	6.41	0.017	12.0	0.260	2.46	6.09	3.30	24.2	7.85	100	38.4	189	45.8	483	110	0.93	29	752	-15.2	314
KBDB-5.03	13.2	0.039	20.7	0.057	1.17	2.84	2.25	26.5	9.49	129	54.9	269	62.2	662	147	0.83	151	825	-5.5	314
KBDB-5.04	7.90	0.056	17.0	0.290	4.40	7.15	3.52	34.5	11.7	145	57.1	278	66.7	718	161	0.67	27	772	-14.4	312
KBDB-5.05	6.26	0.024	10.1	0.250	2.92	4.59	2.83	20.9	6.94	83.6	33.6	161	38.4	403	101	0.87	23	750	-16.1	315
KBDB-5.06	3.95	0.000	2.8	0.003	0.27	0.53	0.21	2.93	1.04	14.9	7.26	40.3	10.8	127	34.1	0.48	127	708	-11.9	325
KBDB-5.07	7.68	0.059	34.5	0.550	9.27	13.1	5.44	59.4	18.9	223	89.4	454	107	1152	263	0.58	25	770	-14.8	307
KBDB-5.08	5.21	0.018	7.6	0.047	0.75	1.91	0.75	10.7	3.93	52.8	23.4	124	30.9	350	86	0.53	92	733	-11.8	321
KBDB-5.09	8.84	0.000	17.5	0.059	1.04	1.82	1.43	16.9	6.73	91.7	39.8	201	49.0	515	121	0.71	177	784	-6.8	312
KBDB-5.11	4.64	0.011	5.7	0.066	0.74	1.86	1.01	10.5	3.42	45.5	18.7	99	23.9	255	61.1	0.76	58	722	-14.1	319
KBDB-5.12	4.36	0.042	12.8	0.210	3.60	4.35	2.44	22.0	7.30	85.5	35.2	177	43.2	469	116	0.69	28	717	-17.1	313
KBDB-5.13	3.47	0.009	4.9	0.059	1.10	1.80	0.86	7.83	2.86	38.5	16.6	87.8	21.9	241	60.8	0.64	40	697	-16.8	319
KBDB-5.14	5.67	0.045	6.5	0.110	2.00	2.66	1.44	16.0	5.20	64.5	26.2	134	30.8	317	76.5	0.63	25	741	-16.3	309
KBDB-5.15	3.61	0.013	6.7	0.120	1.34	1.79	1.58	11.3	3.47	49.2	20.1	103	25.7	281	66.1	0.99	45	700	-16.2	316
KBDB-5.16	5.65	0.004	7.8	0.022	0.37	1.17	0.63	7.17	2.99	42.1	20.5	111	29.1	326	81.1	0.68	229	740	-8.0	312
Granite porphyry (Sample LL-6)																				
LL-6.01	2.36	0.250	7.9	0.100	0.69	1.41	0.36	10.1	3.81	51.1	22.1	111	24.5	255	58.3	0.28	95	665	-15.4	312
LL-6.02	11.73	0.007	15.1	0.070	1.65	3.95	1.36	29.1	11.6	161	69.8	347	76.8	755	167	0.38	75	813	-8.7	308
LL-6.03	3.34	3.820	31.5	1.640	9.93	5.80	1.17	25.7	9.76	127	52.8	257	58.3	597	129	0.20	29	694	-18.2	322

Table 4. Cont.

Analysis	Ti	La	Ce	Pr	Nd	Sm	Eu	Gd	Tb	Dy	Ho	Er	Tm	Yb	Lu	δEu^1	$\text{Ce}^{4+}/\text{Ce}^{3+2}$	T (°C)3	$\log f\text{O}_2 4$	Age (Ma)
LL-6.04	4.07	0.870	22.4	0.300	2.05	3.37	0.73	22.7	9.27	124	54.7	273	62.0	618	141	0.23	100	711	-12.6	308
LL-6.05	2.92	0.093	11.7	0.095	1.17	1.96	0.48	13.1	5.25	70.8	31.7	165	38.9	407	94.0	0.26	99	683	-14.2	311
LL-6.07	3.33	0.071	14.6	0.030	0.77	1.61	0.33	14.0	5.83	82.2	37.0	190	44.6	461	105	0.20	197	693	-11.0	315
LL-6.08	7.83	0.190	10.7	0.099	1.05	2.22	0.45	14.3	5.14	66.0	27.1	133	30.7	311	68.3	0.25	74	772	-10.7	301
LL-6.09	4.00	0.077	16.4	0.088	1.28	3.12	0.81	18.3	7.52	96.8	41.3	204	47.8	472	106	0.33	98	709	-12.8	314
LL-6.10	2.52	0.029	18.4	0.090	1.60	4.19	1.08	25.9	9.51	124	50.3	244	54.2	537	115	0.34	76	670	-15.9	308
LL-6.11	4.73	3.760	21.7	1.290	6.40	2.90	0.35	15.3	5.51	74.5	31.1	158	36.3	361	83.1	0.10	36	724	-15.8	312
LL-6.12	11.0	0.003	13.8	0.055	1.77	3.60	1.57	27.8	11.1	147	64.2	320	72.0	688	153	0.46	66	806	-9.5	305
LL-6.13	7.55	0.059	26.6	0.140	1.89	6.32	3.00	46.5	16.5	211	90.0	430	98.0	937	203	0.62	91	768	-10.1	278
LL-6.14	9.14	0.120	7.4	0.070	0.23	0.65	0.25	6.32	2.33	35.9	15.3	77.7	19.6	190	45.4	0.39	308	787	-4.6	312
LL-6.15	5.42	0.069	11.0	0.092	0.89	1.86	0.51	10.3	4.27	57.7	25.4	131	31.2	317	75.1	0.33	110	736	-10.9	304
LL-6.16	3.29	2.610	14.8	0.940	3.85	2.00	0.29	9.27	3.65	46.9	21.2	109	25.1	259	62.1	0.13	43	692	-16.8	307

¹ Eu anomalies (δEu or $\text{Eu}_N/\text{Eu}_N^*$) are calculated by $\text{Eu}_N/(\text{Sm}_N \times \text{Gd}_N)^{1/2}$, where the element abundances are normalized (N) to the chondrite values from [56]. ² $(\text{Ce}^{4+}/\text{Ce}^{3+})_{\text{Zircon}} = (\text{Ce}_{\text{melt}} - \text{Ce}_{\text{Zircon}}/\text{D}_{\text{Ce(III)}})/(\text{Ce}_{\text{Zircon}}/\text{D}_{\text{Ce(IV)}} - \text{Ce}_{\text{melt}})$, where Ce_{melt} and $\text{Ce}_{\text{Zircon}}$ represent the concentrations of Ce in the whole rock and zircon, respectively, and $\text{D}_{\text{Ce(III)}}$ and $\text{D}_{\text{Ce(IV)}}$ are the zircon–melt distribution coefficients for Ce (III) and Ce (IV), respectively. The $\text{D}_{\text{Ce(III)}}$ and $\text{D}_{\text{Ce(IV)}}$ values can be estimated on the basis of the crystal chemical constraints on trace element partitioning [42]. ³ Ti-in-zircon temperatures are calculated using the equation proposed by [57]: $\log(\text{ppm Ti-in-zircon}) = (5.711 \pm 0.072) - (4800 \pm 86)/T(\text{K}) - \log \alpha_{\text{SiO}_2} + \log \alpha_{\text{TiO}_2}$, where $\alpha_{\text{SiO}_2} = 1$, $\alpha_{\text{TiO}_2} = 0.6$ are used in the calculation. ⁴ Log $f\text{O}_2$ values are calculated using the equation of [58]: $\ln(\text{Ce}/\text{Ce}^*)_{\text{D}} = (0.1156 \pm 0.0050) \times \ln(f\text{O}_2) + (13860 \pm 708)/T(\text{K}) - 6.125 \pm 0.484$.

Table 5. In situ zircon Hf isotopic data on the studied intrusive rocks in the Tuwu-Yandong belt.

Age (Ma)	$^{176}\text{Yb}/^{177}\text{Hf}$	1 σ	$^{176}\text{Lu}/^{177}\text{Hf}$	1 σ	$^{176}\text{Hf}/^{177}\text{Hf}$	1 σ	$\varepsilon\text{Hf}(0)$	$\varepsilon\text{Hf(t)}$	T _{DM1} (Ma)	T _{DM2} (Ma)	f _{Lu/Hf}	
Granodiorite porphyry (sample YD-42)												
YD-42.01	327.8	0.282961	0.000031	0.002289	0.000040	0.063302	0.001156	6.69	13.41	427	480	-0.93
YD-42.03	319.1	0.282985	0.000015	0.002672	0.000034	0.075330	0.001417	7.51	13.98	397	437	-0.92
YD-42.05	316.6	0.282994	0.000016	0.003039	0.000024	0.086979	0.000766	7.86	14.20	386	421	-0.91
YD-42.06	327.6	0.282979	0.000016	0.001839	0.000014	0.048917	0.000515	7.32	14.14	395	434	-0.94
YD-42.07	317.2	0.282980	0.000017	0.002168	0.000007	0.058986	0.000288	7.36	13.89	397	442	-0.93
YD-42.08	329.1	0.282968	0.000021	0.002577	0.000037	0.069694	0.001121	6.92	13.60	421	469	-0.92
YD-42.09	328.5	0.282917	0.000024	0.002525	0.000057	0.070385	0.002180	5.14	11.82	494	583	-0.92
YD-42.10	322.2	0.282922	0.000024	0.002848	0.000045	0.079261	0.001260	5.32	11.80	491	579	-0.91
YD-42.11	320.3	0.282995	0.000021	0.003017	0.000027	0.083928	0.000716	7.88	14.29	385	418	-0.91
YD-42.12	331.9	0.282966	0.000024	0.001973	0.000010	0.053040	0.000367	6.88	13.75	415	462	-0.94
YD-42.13	326.4	0.282927	0.000024	0.002002	0.000021	0.054937	0.000611	5.47	12.22	474	555	-0.94
YD-42.14	323.0	0.282907	0.000022	0.002163	0.000017	0.057937	0.000586	4.79	11.44	504	603	-0.93
YD-42.15	317.2	0.282971	0.000024	0.002410	0.000017	0.068893	0.000583	7.02	13.50	414	466	-0.93
Gabbro (Sample KBDB-5)												
KBDB-5.01	312.3	0.282979	0.000018	0.001580	0.000023	0.039739	0.000557	7.31	13.85	393	440	-0.95
KBDB-5.02	314.1	0.282926	0.000019	0.002726	0.000051	0.072921	0.001285	5.45	11.80	484	573	-0.92
KBDB-5.03	314.1	0.282987	0.000020	0.002880	0.000019	0.075683	0.000721	7.60	13.91	395	438	-0.91
KBDB-5.04	312.2	0.282988	0.000018	0.002380	0.000097	0.063712	0.002737	7.63	14.02	388	429	-0.93
KBDB-5.05	315.4	0.283031	0.000020	0.003164	0.000077	0.084554	0.002326	9.16	15.45	332	340	-0.90
KBDB-5.06	324.9	0.283033	0.000018	0.002244	0.000003	0.052006	0.000117	9.21	15.89	321	319	-0.93
KBDB-5.08	320.6	0.282961	0.000020	0.001466	0.000035	0.034925	0.000742	6.67	13.41	418	475	-0.96
KBDB-5.09	311.9	0.282974	0.000025	0.003441	0.000047	0.092057	0.001463	7.14	13.29	421	476	-0.90
KBDB-5.11	318.7	0.282913	0.000021	0.001967	0.000021	0.050248	0.000545	4.98	11.58	493	591	-0.94
KBDB-5.12	313.0	0.282961	0.000019	0.001376	0.000005	0.035510	0.000169	6.69	13.30	416	476	-0.96
KBDB-5.13	319.0	0.282949	0.000017	0.001536	0.000030	0.038204	0.000806	6.25	12.95	436	503	-0.95
KBDB-5.14	309.1	0.283039	0.000024	0.001994	0.000063	0.054143	0.001597	9.44	15.84	310	310	-0.94
KBDB-5.15	315.8	0.282946	0.000022	0.001380	0.000048	0.034458	0.001262	6.15	12.82	438	509	-0.96
KBDB-5.16	311.6	0.282998	0.000024	0.003428	0.000064	0.092253	0.001661	7.98	14.13	385	422	-0.90
Granite porphyry (Sample LL-6)												
LL-6.01	312.4	0.282924	0.000014	0.001238	0.000015	0.031846	0.000476	5.36	11.98	468	560	-0.96
LL-6.02	308.2	0.282886	0.000015	0.002499	0.000015	0.068273	0.000399	4.05	10.32	540	663	-0.92
LL-6.04	308.0	0.282922	0.000014	0.001759	0.000020	0.047247	0.000485	5.32	11.74	477	572	-0.95
LL-6.05	311.2	0.282957	0.000015	0.001915	0.000036	0.053443	0.000983	6.54	12.99	429	494	-0.94
LL-6.07	315.0	0.282951	0.000015	0.002088	0.000027	0.055130	0.000691	6.34	12.84	439	507	-0.94

Table 5. Cont.

	Age (Ma)	$^{176}\text{Yb}/^{177}\text{Hf}$	1σ	$^{176}\text{Lu}/^{177}\text{Hf}$	1σ	$^{176}\text{Hf}/^{177}\text{Hf}$	1σ	$\varepsilon\text{Hf}(0)$	$\varepsilon\text{Hf}(t)$	$T_{\text{DM}1}$ (Ma)	$T_{\text{DM}2}$ (Ma)	$f_{\text{Lu/Hf}}$
LL-6.08	300.9	0.282928	0.000013	0.001488	0.000017	0.041042	0.000537	5.53	11.85	465	559	-0.96
LL-6.09	314.0	0.282949	0.000014	0.002322	0.000052	0.061957	0.001479	6.27	12.70	445	515	-0.93
LL-6.11	311.7	0.282941	0.000016	0.001740	0.000039	0.048441	0.001060	5.96	12.46	450	529	-0.95
LL-6.12	305.2	0.282919	0.000016	0.002668	0.000024	0.071948	0.000565	5.21	11.39	493	592	-0.92
LL-6.14	312.2	0.282919	0.000014	0.002172	0.000102	0.060654	0.002872	5.20	11.62	487	583	-0.93
LL-6.16	306.6	0.282933	0.000014	0.001995	0.000035	0.055510	0.001044	5.68	12.03	465	553	-0.94

Note: $\varepsilon\text{Hf}(0) = [({}^{176}\text{Hf}/{}^{177}\text{Hf})_S / ({}^{176}\text{Hf}/{}^{177}\text{Hf})_{\text{CHUR},0} - 1] \cdot 10000$; $\varepsilon\text{Hf}(t) = [({}^{176}\text{Hf}/{}^{177}\text{Hf})_S - ({}^{176}\text{Lu}/{}^{177}\text{Hf})_S \cdot (e^{\lambda t} - 1)] / [({}^{176}\text{Hf}/{}^{177}\text{Hf})_{\text{CHUR},0} - ({}^{176}\text{Lu}/{}^{177}\text{Hf})_{\text{CHUR},0} \cdot (e^{\lambda t} - 1)] - 1] \cdot 10000$; $T_{\text{DM}1} = 1/\lambda \cdot \ln\{1 + [({}^{176}\text{Hf}/{}^{177}\text{Hf})_S - ({}^{176}\text{Hf}/{}^{177}\text{Hf})_{\text{DM}}]/[({}^{176}\text{Lu}/{}^{177}\text{Hf})_S - ({}^{176}\text{Lu}/{}^{177}\text{Hf})_{\text{DM}}]\}$; $T_{\text{DM}2} = T_{\text{DM}1} - (T_{\text{DM}1} - t) \cdot (f_{\text{cc}} - f_s) \cdot (f_{\text{cc}} - f_{\text{DM}})$; $f_{\text{Lu/Hf}} = [({}^{176}\text{Lu}/{}^{177}\text{Hf})_S / ({}^{176}\text{Lu}/{}^{177}\text{Hf})_{\text{CHUR},0}] - 1$, where $({}^{176}\text{Hf}/{}^{177}\text{Hf})_S$ and $({}^{176}\text{Lu}/{}^{177}\text{Hf})_S$ are the measured values of the samples, s = sample, and t = crystallization time of zircon; $({}^{176}\text{Lu}/{}^{177}\text{Hf})_{\text{CHUR},0} = 0.0332$ and $({}^{176}\text{Hf}/{}^{177}\text{Hf})_{\text{CHUR},0} = 0.282772$ [59]; $({}^{176}\text{Lu}/{}^{177}\text{Hf})_{\text{DM}} = 0.0384$ and $({}^{176}\text{Hf}/{}^{177}\text{Hf})_{\text{DM}} = 0.28325$ [60]; $f_{\text{cc}} = -0.55$ and $f_{\text{DM}} = 0.16$; and $\lambda = 1.867 \times 10^{-12}/\text{yr}^{-1}$ [61] were used in the calculation.

Table 6. Sr–Nd isotopic compositions of the studied intrusive rocks in the Tuwu-Yandong belt.

Sample No.	Rock Type	Rb (ppm)	Sr (ppm)	Age-Corrected (Ma)	$^{87}\text{Rb}/^{86}\text{Sr}$	$^{87}\text{Sr}/^{86}\text{Sr}$	I_{Sr}	Sm (ppm)	Nd (ppm)	$^{147}\text{Sm}/^{144}\text{Nd}$	$^{143}\text{Nd}/^{144}\text{Nd}$	$f_{\text{Sm/Nd}}$	T_{DM} (Ma)	$\varepsilon\text{Nd}(0)$	$\varepsilon\text{Nd}(t)$
YD-42	GDP	15.9	234	322	0.20	0.704706	0.703804	1.44	7.9	0.110252416	0.512782	-0.44	545	2.81	6.37
YD-46	GDP	16.3	327	322	0.14	0.704614	0.703953	1.93	11.1	0.105558435	0.512777	-0.46	528	2.71	6.46
YD-55-4-95	GDP	18.2	371	322	0.14	0.704457	0.703807	2.18	11.7	0.112719352	0.512802	-0.43	528	3.20	6.66
KBDB-5	GA	9.5	287	314	0.10	0.704312	0.703882	3.87	16.3	0.143313503	0.512898	-0.27	549	5.07	7.23
KBDB-6	GA	15.7	328	314	0.14	0.704302	0.703681	2.67	10.6	0.153084279	0.512895	-0.22	645	5.01	6.77
KBDB-7	GA	19.4	361	314	0.16	0.704510	0.703814	2.79	11.3	0.149789057	0.512881	-0.24	646	4.74	6.63
LL-5	GP	28.8	253	310	0.33	0.706449	0.704998	2.50	13.8	0.109001497	0.512705	-0.45	651	1.31	4.78
LL-6	GP	38.4	215	310	0.52	0.707114	0.704830	2.87	15.7	0.110302932	0.512724	-0.44	631	1.68	5.10
LL-9	GP	52.8	314	310	0.49	0.706689	0.704544	2.35	13.0	0.109035708	0.512727	-0.45	619	1.74	5.21
LL-10	GP	52.2	320	310	0.47	0.706758	0.704672	2.87	14.7	0.11763931	0.512718	-0.4	688	1.56	4.69

Abbreviation: GDP, granodiorite porphyry; GA, gabbro; GP, granite porphyry. $({}^{87}\text{Sr}/{}^{86}\text{Sr})_i = ({}^{87}\text{Sr}/{}^{86}\text{Sr})_s - (87\text{Rb}/86\text{Sr})_s \cdot (e^{\lambda t} - 1)$; ${}^{87}\text{Sr}/{}^{86}\text{Sr} = (\text{Rb/Sr}) \times 2.8956$; $\lambda_{\text{Rb-Sr}} = 1.42 \times 10^{-11}/\text{a}$; $({}^{143}\text{Nd}/{}^{144}\text{Nd})_i = ({}^{143}\text{Nd}/{}^{144}\text{Nd})_s - ({}^{147}\text{Sm}/{}^{144}\text{Nd})_s \cdot (e^{\lambda t} - 1)$; ${}^{147}\text{Sm}/{}^{144}\text{Nd} = (\text{Sm/Nd}) \times 0.60456$; $\lambda_{\text{Sm-Nd}} = 6.54 \times 10^{-12}/\text{a}$; $\varepsilon\text{Nd}(t) = 10,000 [({}^{143}\text{Nd}/{}^{144}\text{Nd})_i / ({}^{143}\text{Nd}/{}^{144}\text{Nd})_{\text{CHUR}(t)} - 1]$; $({}^{143}\text{Nd}/{}^{144}\text{Nd})_{\text{CHUR}(t)} = ({}^{143}\text{Nd}/{}^{144}\text{Nd})_{\text{CHUR}(0)} - ({}^{147}\text{Sm}/{}^{144}\text{Nd})_{\text{CHUR}} \cdot (e^{\lambda t} - 1)$; $({}^{143}\text{Nd}/{}^{144}\text{Nd})_{\text{CHUR}(0)} = 0.512638$; $({}^{147}\text{Sm}/{}^{144}\text{Nd})_{\text{CHUR}} = 0.1967$; $T_{\text{DM}} = 1/\lambda \times \ln\{1 + [({}^{143}\text{Nd}/{}^{144}\text{Nd})_s - ({}^{143}\text{Nd}/{}^{144}\text{Nd})_{\text{DM}}] / [({}^{147}\text{Sm}/{}^{144}\text{Nd})_s - ({}^{147}\text{Sm}/{}^{144}\text{Nd})_{\text{DM}}]\}$; $({}^{147}\text{Sm}/{}^{144}\text{Nd})_{\text{DM}} = 0.21357$; $({}^{143}\text{Nd}/{}^{144}\text{Nd})_{\text{DM}} = 0.51315$; $({}^{147}\text{Sm}/{}^{144}\text{Nd})_{\text{crust}} = 0.118$ [11]; $({}^{87}\text{Sr}/{}^{86}\text{Sr})_s$; and $({}^{143}\text{Nd}/{}^{144}\text{Nd})_s$ are the measured values of the samples.

5. Discussion

5.1. Timing of the Tuwu-Yandong Belt

The precise dating of intrusive rocks may be used to constrain the timing and duration of magmatic events, which is crucially important for understanding the rock-forming process and geodynamic setting [21,62,63]. Based on our new LA-ICP-MS zircon U-Pb data, the granodiorite porphyry, gabbro, and granite porphyry from the Tuwu-Yandong belt were formed at 321.8 ± 3.1 Ma, 313.5 ± 1.2 Ma, and 309.8 ± 2.5 Ma, respectively. In recent decades, a large number of geochronological studies on metallogenic age, mineralized porphyry, and pre- and post-mineralization granitic intrusive rocks have been completed [5,10,13,14,19,20,22,64–67]. These studies, together with this study, reveal that Carboniferous intrusive magmatism events have widely taken place in the Tuwu-Yandong belt, ranging from 348 Ma to 310 Ma (Table 7 and references therein). On the basis of these available geochronological data and their magmatic associations, three major intrusive episodes have been identified: (1) the earliest intermediate intrusive rocks (e.g., diorite or diorite porphyry) emplaced at ca. 348–338 Ma [5,10,19]; (2) the felsic intrusive rocks, some of which show adakitic features (e.g., plagiogranite porphyry or tonalite porphyry [5,22,23]; granodiorite porphyry (this study); and porphyritic granodiorite [14]), formed during ca. 335–315 Ma ([5,10,13,14,19–22]; this study); and 3) the latest mafic (gabbro) and felsic (e.g., K-feldspar granite, granite porphyry) intrusive rocks, showing an interrupted sequence of SiO_2 values that are similar to typical bimodal values (Figure 4a), formed at ca. 314–310 Ma ([67]; this study).

In addition, previous studies have reported numerous molybdenite Re-Os ages (322.7 ± 2.3 Ma [68] for the Tuwu-Yandong deposits; 343 ± 26 Ma [69], 331.3 ± 2.1 Ma [5], 324.3 ± 2.7 Ma [17], and 326.2 ± 4.5 Ma [70] for the Yandong deposit; 335.8 ± 3.3 Ma [4] and 334.1 ± 3.3 Ma [15] for the Tuwu deposit; 316.8 ± 3.7 Ma [15] for the Linglong deposit; 317.0 ± 3.6 Ma [15] for the Chihu deposit) and sericite Ar-Ar ages (332.8 ± 3.8 Ma for the Yandong deposit [17] and 328.1 ± 1.4 Ma for the Tuwu deposit [16]), suggesting that porphyry Cu mineralization in the Tuwu-Yandong belt may have occurred during 343–317 Ma (Table 7). Two periods (ca. 335–330 Ma and 323–315 Ma) of porphyry Cu mineralization have also been identified in the belt, according to the geochronological data on the Cu mineralization and ore-related intrusive magmatism [15]. In this study, the granodiorite porphyry may be genetically related to the second episode of porphyry Cu mineralization, while the gabbro and granite porphyry most likely formed after the Cu mineralization, which is consistent with the spatial relationship between these intrusive rocks and Cu deposits (Figure 2).

Table 7. Isotopic age data in the Tuwu-Yandong porphyry Cu belt.

Locations.	Dating Samples	Dating Methods	Ages (Ma)	References
Fuxing	Plagiogranite porphyry	SIMS zircon U-Pb	332.1 ± 2.2	[21]
	Monzogranite	SIMS zircon U-Pb	328.4 ± 3.4	[21]
Yandong	Plagiogranite porphyry	LA-ICP-MS zircon U-Pb	334.9 ± 2.2	[71]
	Diorite	LA-ICP-MS zircon U-Pb	348.3 ± 6	[10]
	Diorite porphyry	SIMS zircon U-Pb	340 ± 3	[19]
	Diorite porphyry	SIMS zircon U-Pb	338.6 ± 2.9	[5]
	Plagiogranite porphyry	SHRIMP zircon U-Pb	333 ± 4	[64]
	Plagiogranite porphyry	SIMS zircon U-Pb	332.2 ± 2.3	[19]
	Plagiogranite porphyry	SHRIMP zircon U-Pb	335 ± 3.7	[65]
	Plagiogranite porphyry	LA-ICP-MS zircon U-Pb	339.3 ± 2.2	[10]
	Plagiogranite porphyry	SIMS zircon U-Pb	335.3 ± 2.9	[5]
	Granodiorite porphyry	LA-ICP-MS zircon U-Pb	321.8 ± 3.1	This study
	Quartz albite porphyry	LA-ICP-MS zircon U-Pb	323.6 ± 2.5	[10]
	Quartz porphyry	LA-ICP-MS zircon U-Pb	324.1 ± 2.3	[10]
	Quartz porphyry	SIMS zircon U-Pb	327.6 ± 2.6	[5]

Table 7. Cont.

Locations.	Dating Samples	Dating Methods	Ages (Ma)	References
Tuwu-Yandong	Molybdenite	Re-Os isochron	343 ± 26	[69]
	Molybdenite	Re-Os isochron	331.3 ± 2.1	[5]
	Phyllitic-altered plagiogranite porphyry	Sericite Ar-Ar plateau	332.8 ± 3.8	[17]
		Re-Os mean	324.3 ± 2.7	[17]
		Molybdenite Re-Os model	326.2 ± 4.5	[70]
		Re-Os isochron	322.7 ± 2.3	[68]
	Plagiogranite porphyry	SHRIMP zircon U-Pb	334 ± 3	[64]
	Plagiogranite porphyry	SIMS zircon U-Pb	334.7 ± 3	[72]
	Plagiogranite porphyry	SIMS zircon U-Pb	332.8 ± 2.5	[20]
	Plagiogranite porphyry	SHRIMP zircon U-Pb	332.3 ± 5.9	[22]
Tuwu	Gabbro	LA-ICP-MS zircon U-Pb	314.7 ± 3.4	This study
	Molybdenite	Re-Os isochron	335.8 ± 3.3	[4]
Linglong	Phyllitic-altered plagiogranite porphyry	Sericite Ar-Ar plateau	328.1 ± 1.4	[16]
		Re-Os isochron	334.1 ± 3.3	[15]
	Quartz albite porphyry	SIMS zircon U-Pb	318.6 ± 3.0	[13]
	Granite porphyry	LA-ICP-MS zircon U-Pb	309.8 ± 2.5	This study
Chihu	Molybdenite	Re-Os isochron	316.8 ± 3.7	[15]
	Plagiogranite porphyry	SHRIMP zircon U-Pb	322 ± 10	[66]
	Granodiorite	SIMS zircon U-Pb	320.2 ± 2.4	[14]
	Porphyritic granodiorite	SIMS zircon U-Pb	314.5 ± 2.5	[14]
	K-feldspar granite	LA-ICP-MS zircon U-Pb	311 ± 3	[67]
	Molybdenite	Re-Os isochron	317.0 ± 3.6	[15]

5.2. Magma Oxidation State

It is widely accepted that highly oxidized magmas are favorable for porphyry Cu (Mo) mineralization (e.g., [3,73]). Oxidized magmas can extract more Cu (and Mo) from source rocks during melting and scavenge sulfides during ascent [74]. A high oxygen fugacity also prevents the sulfide precipitation, and metals (e.g., Cu, Mo) remain in the exsolved aqueous phase for the later porphyry Cu mineralization ([75]).

Zircon (ZrSiO_4) is an exceptionally robust mineral that retains its primary chemical and isotopic compositions from the time of crystallization and provides chemical information on the parental magmas [3]. Unlike other REEs that have only +3 valency, Ce and Eu commonly have two oxidation states in terrestrial magmas, and zircon more preferentially incorporates the oxidized cations Ce^{4+} (0.97 Å) and Eu^{3+} (1.07 Å) into the Zr^{4+} (0.84 Å) site of its structure than the reduced Ce^{3+} (1.14 Å) and Eu^{2+} (1.25 Å) [75]. Thus, high $\text{Ce}^{4+}/\text{Ce}^{3+}$ and Eu/Eu^* (also known as δEu) ratios usually reflect the high oxygen fugacity ($f\text{O}_2$) of the parental magmas, which were used to quantify the oxidized nature of the parental magmas associated with porphyry deposits in northern Chile [42], Tibet ($\text{Ce}^{4+}/\text{Ce}^{3+} > 120$ and $\delta\text{Eu} > 0.4$ [76,77]), and Qinling [78] in China. Recent research has also demonstrated that porphyry Cu deposits of large (>4 Mt Cu) and intermediate (1.5–4 Mt Cu) sizes are associated with granitic intrusions with zircon $\text{Ce}^{4+}/\text{Ce}^{3+}$ ratios of >120, whereas the ratios are 54–69 for the small porphyry deposits in the CAOB [3,79].

In this study, the zircon $\text{Ce}^{4+}/\text{Ce}^{3+}$ ratios of the granodiorite porphyry (avg. 129, median = 112, $n = 15$) are higher than those of the gabbro (avg. 74, median = 40, $n = 15$) and granite porphyry (avg. 100, median = 91, $n = 15$), both of which are consistent with those of the granitic intrusions associated with large and medium porphyry Cu deposits in the CAOB (Figure 11a,c; [10]). The samples of the granodiorite porphyry (and plagiogranite porphyry [10]) are mainly plotted between the fayalite–magnetite–quartz (FMQ) buffer curve and the magnetite–hematite (MH) buffer curve in the temperature (T) vs. $\log f\text{O}_2$ diagram (Figure 11d; [74,80]), further indicating the high $f\text{O}_2$ of the parental magmas. However, the low zircon Eu/Eu^* ratios (<0.4) of the granodiorite porphyry (and plagiogranite porphyry [10]) suggest that the Eu/Eu^* ratios of the zircon grains may be

affected by another factor in addition to the oxidation conditions of the parental magmas. Since Eu^{2+} is preferentially incorporated into the Ca^{2+} site of plagioclase, the crystallization of plagioclase lowers the Eu in the residual melt and results in low Eu/Eu^* in any late-crystallizing phases after plagioclase [3]. Indeed, the presence of plagioclase phenocrysts in the granodiorite porphyry (Figure 3b,c) suggests that the plagioclase crystallized early and preferentially removed Eu^{2+} from the melt to cause low Eu/Eu^* ratios in the zircon grains. Therefore, the low Eu anomalies in the zircon is not in conflict with the high $\text{Ce}^{4+}/\text{Ce}^{3+}$ in the zircon grains [3]. In addition, the lower magma temperature of the granodiorite porphyry (avg. 688°C , median = 673°C , $n = 15$; determined by the Ti-in-zircon thermometry) compared to that of the gabbro (avg. 742°C , median = 740°C , $n = 15$) and granite porphyry (avg. 728°C , median = 711°C , $n = 15$) suggests that the parental magmas of the granodiorite porphyry may be water-rich and based on a lower water fugacity ($f_{\text{H}_2\text{O}}$) reflecting the higher magma temperature [79]. Thus, the granodiorite porphyry (321.8 ± 3.1 Ma) was likely derived from a more oxidized and hydrous magma source than the gabbro and granite porphyry, implying its Cu fertility and capacity to form medium-large porphyry Cu deposits [3]. The copper mineralization potential is further supported by the molybdenite Re-Os age of 323–317 Ma in the Tuwu-Yandong porphyry Cu belt [15,68].

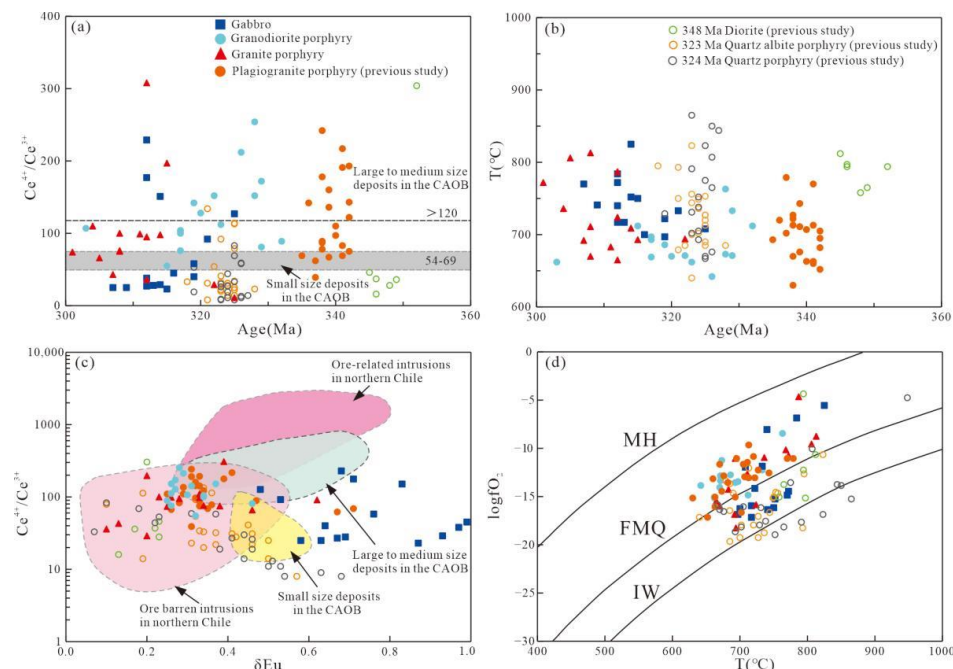


Figure 11. (a) Zircon age vs. $\text{Ce}^{4+}/\text{Ce}^{3+}$ ratios; (b) zircon age vs. T ; (c) Zircon δEu vs. $\text{Ce}^{4+}/\text{Ce}^{3+}$ ratios and (d) T vs. $\log f\text{O}_2$ [58,74]. Data on the ore-related/barren intrusions in northern Chile are from [37]. Data on the medium-large and small porphyry deposits in the CAOB are from [3]. The data on the diorite, plagiogranite porphyry, quartz albite porphyry, and quartz porphyry of the Tuwu-Yandong deposits are from [10].

5.3. Petrogenesis and Magma Source

5.3.1. The Adakitic Granodiorite Porphyry

Several petrogenetic models have been proposed to interpret the origins of adakites or adakitic rocks, such as (1) the partial melting of a subducted oceanic crust with or without contributions from a mantle wedge [52,81]; (2) partial melting of a thickened mafic lower crust [82]; (3) partial melting of a delaminated continental lower crust [83]; and (4) the crustal assimilation and fractional crystallization (AFC) of parental basaltic magmas [84]. Adakitic rocks derived from lower crust have high $(^{87}\text{Sr}/^{86}\text{Sr})_i$ and low $\text{Mg}^{\#}$, $\varepsilon\text{Nd(t)}$, and $\varepsilon\text{Hf(t)}$ values [85,86], and those from the AFC processes of parental basaltic

magmas show significant systematic variations in their geochemistry and Sr–Nd isotopic compositions [87]. However, the adakitic granodiorite porphyry has $Mg^{\#}$ (47.4–58.1), low and uniform ($^{87}\text{Sr}/^{86}\text{Sr}$)_i (0.703804–0.703953), and high and uniform $\varepsilon\text{Nd(t)}$ (6.37–6.66) and $\varepsilon\text{Hf(t)}$ values (11.4–14.3), as well as a narrow range of compositions (65.94–67.86 wt.% SiO_2) and no mafic enclaves, which is inconsistent with the adakites of the latter three origins.

The granodiorite porphyry samples are strongly enriched in LREE relative to HREE ([La/Yb]_N = 6.8–9.5) (Figure 5a) and show clear depletion in Nb, Ta, and Ti and positive Ba, U, K, and Sr anomalies (Figure 5b) similar to those of most modern subduction-related magmatic rocks [88,89]. The subduction-unrelated magmas are mostly plotted within yhr MORB-OIB array in the Th/Yb versus Nb/Yb diagram (Figure 12a), whereas those of the subduction zone show a significant shift away from the mantle array. The granodiorite porphyry samples possess elevated Th/Yb ratios, indicating their subduction-related enrichment. Their high Ba (188–419 ppm) and Ba/Th (mainly >170) values and low Th (<1.5 ppm) and Th/Nb (<0.6) ratios (Figure 12c) further indicate that the parental magmas of the granodiorite porphyry may be metasomatized by slab-derived fluids [84]. In the $Mg^{\#}$ versus SiO_2 diagram (Figure 6b), the granodiorite porphyry samples plot within the field of the subducted slab-derived adakites. Furthermore, the La/Sm ratios of the granodiorite porphyry show a positive correlation with the La contents, implying that the partial melting process was dominant in the petrogenesis (Figure 12d). These geochemical and isotopic signatures indicate that the granodiorite porphyry was most likely derived from the partial melting of a subducting oceanic crust rather than the partial melting of a delaminated lower crust or thickened mafic lower crust or the AFC process of basaltic magmas.

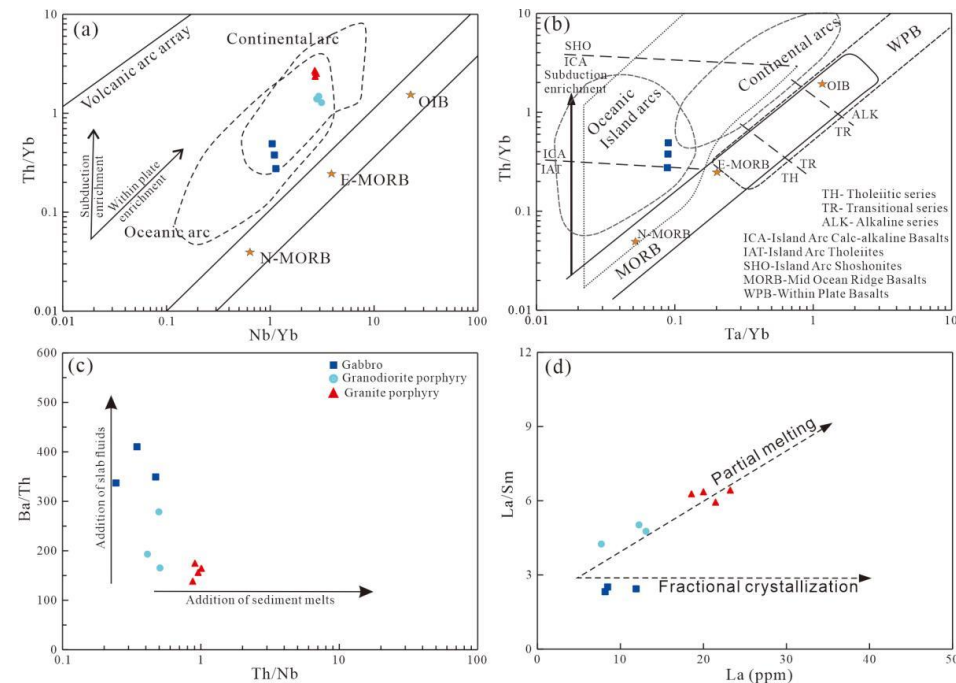


Figure 12. (a) Th/Yb vs. Nb/Yb diagram (after [90]), (b) Th/Yb vs. Ta/Yb diagram (after [91]), (c) Ba/Th vs. Th/Nb diagram, and (d) La/Sm vs. La diagram of the intrusive rocks in the Tuwu-Yandong belt. N-MORB and E-MORB, respectively, represent the normal and enriched mid-ocean ridge basalts, and OIB represents the ocean island basalts.

Melts derived from the crust are characterized by $Mg^{\#}$ values of less than 40 regardless of the degree of melting, whereas those generated from the mantle exhibit high $Mg^{\#}$ values (greater than 40) [13,22]. In general, the reaction of slab-derived melts with overlying peridotite in the mantle wedge can result in the high $Mg^{\#}$ values [5,52]. Therefore, we speculate that the formation of the granodiorite porphyry may involve the addition of mantle-derived components. The granodiorite porphyry samples have low ($^{87}\text{Sr}/^{86}\text{Sr}$)_i

ratios and positive $\epsilon\text{Nd(t)}$, which, in part, overlap with the mantle array in the $\epsilon\text{Nd(t)}$ versus $(^{87}\text{Sr}/^{86}\text{Sr})_i$ diagram (Figure 10c), and positive $\epsilon\text{Hf(t)}$ values, which fall between the depleted mantle (DM) and the 0.88 Ga crustal evolution line, as well as young Hf crustal (single-stage) model ages (385–504 Ma), further reflecting the interaction between melts generated from a subducted oceanic slab and mantle melts. The petrogenesis of the granodiorite porphyry (ca. 322 Ma) is similar to that of adakitic plagiogranite porphyry (ca. 335–332 Ma, [5,22,23]) in the Tuwu-Yandong belt.

5.3.2. The High-Al Gabbro

The gabbro samples are characterized by low SiO_2 contents (49.08–52.02 wt.%) and high MgO (5.62–7.00 wt.%), Fe_2O_3^T (9.10–9.74 wt.%), V (209–281 ppm), Cr (107–172 ppm), and Ni (36–77) contents and $\text{Mg}^\#$ values (53.3–59.9), suggesting that they are unlikely to have originated from the lower crust [92] or the mantle-derived primary magma (usually with MgO contents > 15 wt.%, $\text{Mg}^\#$ > 65, Cr > 2000 ppm, and Ni > 500 ppm) [93] but rather from an evolved magma. They have low $(^{87}\text{Sr}/^{86}\text{Sr})_i$ and high $\epsilon\text{Nd(t)}$ (6.63–7.23) and $\epsilon\text{Hf(t)}$ (11.6–15.9) values, as well as young Nd ($T_{\text{DM}} = 549$ –646 Ma) and Hf ($T_{\text{DM1}} = 310$ –493 Ma, $T_{\text{DM2}} = 310$ –591 Ma) model ages, reflecting a depleted mantle source, which is supported by the $(^{87}\text{Sr}/^{86}\text{Sr})_i$ vs. $\epsilon\text{Nd(t)}$ diagram (Figure 10c). These geochemical and isotopic signatures indicate that the gabbro was most likely derived from the partial melting of the mantle peridotite. The ratios of REE are useful criteria for constraining the composition of the mantle source and degree of partial melting [93]. Experimental studies have shown that the partition coefficients of REE are different for garnet- and spinel-facies peridotites. The HREE is commonly preferentially retained by garnet, while spinel preferentially incorporates the MREE [94]. The gabbro samples exhibit moderate $[\text{La}/\text{Yb}]_N$ (2.7–3.0) and low $[\text{Dy}/\text{Yb}]_N$ (ca. 1.1) ratios with fairly flat REE patterns, probably indicating their formation at the depth of the spinel stability field.

The gabbro samples exhibit an enrichment in LILEs (e.g., Ba, U, K, and Sr) and depletion in HFSEs (Nb, Ta, and Ti), which may be ascribed to the partial melting of a depleted mantle wedge with the addition of slab-derived components (fluids or melts) [95], which is further supported by the elevated Th/Yb ratios (Figure 12a,b) [90,91]. If the depleted mantle wedge peridotite is modified by a low level of slab-derived melts, it will produce high-Nb or Nb-enriched basaltic rocks [94], which is inconsistent with the studied gabbro, which has low Nb (2.08–3.23) abundances. The gabbro samples have high and variable Ba/Th (337–410) but low and constant Th/Nb (0.24–0.47) ratios, strongly suggesting that the subduction components were dominated by slab-derived hydrous fluids instead of sediments (Figure 12c). In addition, the gabbro samples possess a narrow La/Sm ratio range with variable La contents (Figure 12d), suggesting that the magma that formed the gabbro underwent significant fractional crystallization. The positive correlations of CaO , Cr, and Ni with $\text{Mg}^\#$ and negative correlation of MgO with SiO_2 (Table 2) are consistent with the fractionation of olivine, pyroxene, or amphibole. The positive Eu and Sr anomalies (Figure 5a,b) and high Al_2O_3 contents (Table 2) argue against plagioclase fractionation. Therefore, the gabbro was likely derived from the partial melting of a depleted mantle wedge hydrated by slab-released fluids, and the parental magma underwent the crystal fractionation of Al-poor phases such as olivine, pyroxene, or amphibole, resembling high-alumina basalt that was formed by the fractional crystallization of mantle-derived hydrous magma [25].

5.3.3. The Non-Fractionated I-Type Granite Porphyry

The granite porphyry samples are characterized by relatively low 10,000 Ga/Al (1.37–1.53), Zr + Nb + Y + Ce (116–187 ppm), $\text{K}_2\text{O} + \text{Na}_2\text{O}$ (<8 wt.%), and $\text{Fe}_2\text{O}_3^T/\text{MgO}$ (1.20–1.56) values, falling into the field of non-fractionated granites (Figure 13a,b; [96]). They possess calculated Ti-in-zircon temperatures [57] in the range of 665–813 °C (avg. 728 °C, median = 711 °C, $n = 16$), which contrast the high-temperature formation conditions of A-type granites (>800 °C, [97]). Moreover, A-type granites generally contain

some special alkali mafic minerals, such as arfvedsonite, sodium pyroxene, riebeckite, and late-crystallizing biotite and amphibole [98]. However, these mineral assemblages were not identified in our petrographical observations (Figure 3). Therefore, the petrological and geochemical features rule out an affinity with A-type granites. The granite porphyry samples show a negative correlation between the P_2O_5 and SiO_2 contents (Figure 13c) and positive correlation between the Y and Rb values (Figure 13d), which are typical I-type granite evolution trends [99]. Furthermore, the absence of aluminous minerals (e.g., muscovite, tourmaline, and garnet [100]), low A/CNK ratios of 1.01–1.09 (Figure 4d), and high Na_2O contents of 5.08–5.25 wt.% indicate that the granite porphyry is I-type rather than S-type, which commonly contains Al-rich minerals with high A/CNK values (>1.1) and low Na_2O contents [101]. Therefore, we classify the granite porphyry as the non-fractionated I-type rather than the S- or A-type.

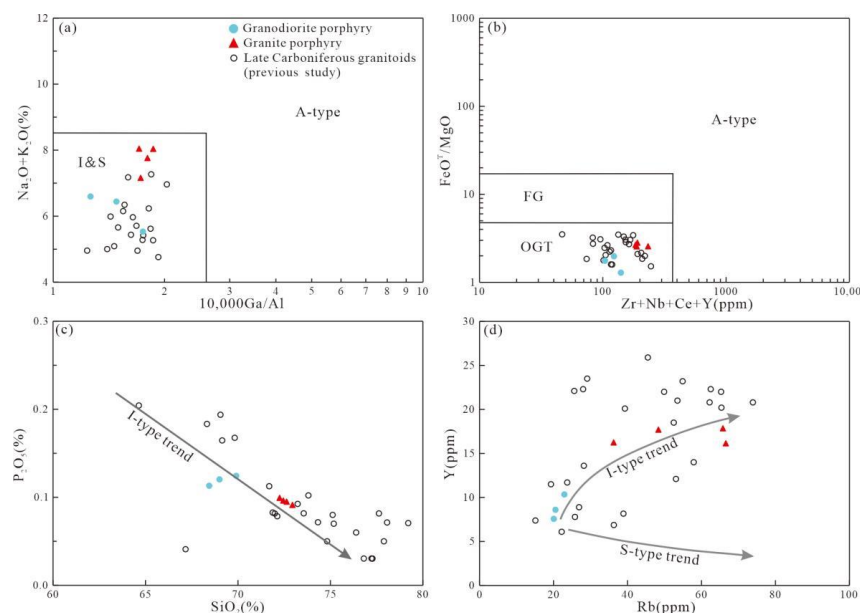


Figure 13. Discrimination diagrams for the genetic type of the granitoids in the Tuwu-Yandong belt. (a) $Na_2O + K_2O$ vs. $10,000 Ga/Al$ diagram [96]; (b) FeO^T/MgO vs. $Zr + Nb + Ce + Y$ diagram [96]; (c) P_2O_5 vs. SiO_2 diagram; (d) Y vs. Rb diagram [99]. FG, fractionated felsic granites; OGT, unfractionated M-, I-, and S-type granites. The data from previous studies can be found in Supplementary Table S1.

Prior studies uncovered that I-type granitoids may be formed by three petrogenetic scenarios, including (1) a complete process of fractional crystallization from primary mafic magmas [102]; (2) the mixing of crustal-derived materials with mantle-derived magmas [103]; and (3) the partial melting of intermediate to mafic metagranitic rocks without sedimentary contamination [104]. The non-fractionated I-type granite porphyry samples contain lower MgO (<0.9 wt.%), Cr (5.6–14.3 ppm), and Ni (1.6–4.7 ppm) contents but higher SiO_2 (>71 wt.%) contents compared with the magmas derived from the direct partial melting of the mantle, which generally possess high Mg[#] values and exhibit mafic to intermediate compositions [105]. The absence of mafic microgranitoid enclaves in the rocks and consistent Sr–Nd isotopic compositions (Figure 10c) indicate that the mixing of mafic and silicic melts is unlikely to have occurred. The La/Sm ratios of the granite porphyry samples are positively correlated with the La contents, implying that the granite porphyry was likely formed by partial melting (Figure 12e). The Mg[#] (38.7–41.0) of the granite porphyry samples resemble those of the experimental melts from the metabasalts and eclogites (Figure 6b), suggesting that the magma may have been formed by the partial melting of a mafic crustal source. The Th/La ratios (0.23–0.29) of the granite porphyry samples are close to the average Th/La ratio of the crust (~0.3 [106]) but higher than that of the

mantle (~0.12 [51,107]), further indicating a crustal origin. The granite porphyry samples have high $\epsilon\text{Hf(t)}$ (10.3–13.0; Figure 10a,b) and $\epsilon\text{Nd(t)}$ values (4.78–5.21) (Figure 10c,d) and young Hf ($T_{\text{DM1}} = 429\text{--}540\text{ Ma}$, $T_{\text{DM2}} = 494\text{--}663\text{ Ma}$; Table 5) and Nd ($T_{\text{DM1}} = 619\text{--}688\text{ Ma}$; Table 6) model ages. These geochemical and isotopic signatures demonstrate that the granite porphyry was likely derived from the juvenile lower crust. Their U-shaped REE patterns (low $[\text{Dy}/\text{Yb}]_{\text{N}}$ = 0.83–0.94) and relatively high Y and Yb contents (Figure 5a) indicate that amphibole (rather than garnet) acts as a residual phase during crustal melting [25].

5.4. Tectonic Implications

The eastern Tianshan orogenic belt occupies the middle part of the CAOB, constituting an important Cu–Mo–Au–Ni–Fe–Ag metallogenic province in China [4,14]. Previous studies have revealed that the eastern Tianshan orogenic belt underwent a long and complex tectonic evolution during the Paleozoic to Mesozoic, including subduction and accretion followed by the collision of the Siberian and Tarim Cratons, and post-collision extension [25,108]. Recently, a large number of Late Ordovician–Late Carboniferous magmatic rocks with arc affinity have been reported in the Dananhu island arc belt, such as Yudai diorite porphyry ($452.7 \pm 2.8\text{ Ma}$ [7]), Sanchakou-Yuhai diorites and granodiorites (444–430 Ma and 325–318 Ma, respectively, [8,9,79,109,110]), and Tuwu-Yandong intrusive rocks (348–315 Ma; Table 7), which are interpreted to be related to the northward subduction of the ancient Tianshan Ocean (e.g., Kangguer Ocean). The studied granodiorite porphyry (322 Ma) and granite porphyry (310 Ma) have relatively low Y, Yb, Ta, Nb, and Rb contents which are similar to those of typical oceanic volcanic arc granites (Figure 14a–c). The studied gabbro samples are plotted in the field of the island arc basalt in the Th–Ta–Hf/3 diagram (Figure 14d [111]), and on the Th/Yb vs. Nb/Yb diagram and the Ta/Yb–Th/Yb diagram (Figure 12a,b), all the intrusive rock samples fall into the “Oceanic Arcs” field. Consequently, these Late Carboniferous intrusions in the Tuwu-Yandong belt most likely formed in an island arc setting. Nevertheless, the subduction process of the ancient oceanic basin during the Late Carboniferous remains controversial, with the proposed processes including slab rollback, flat subduction, and ridge subduction [10,25,39,105,112].

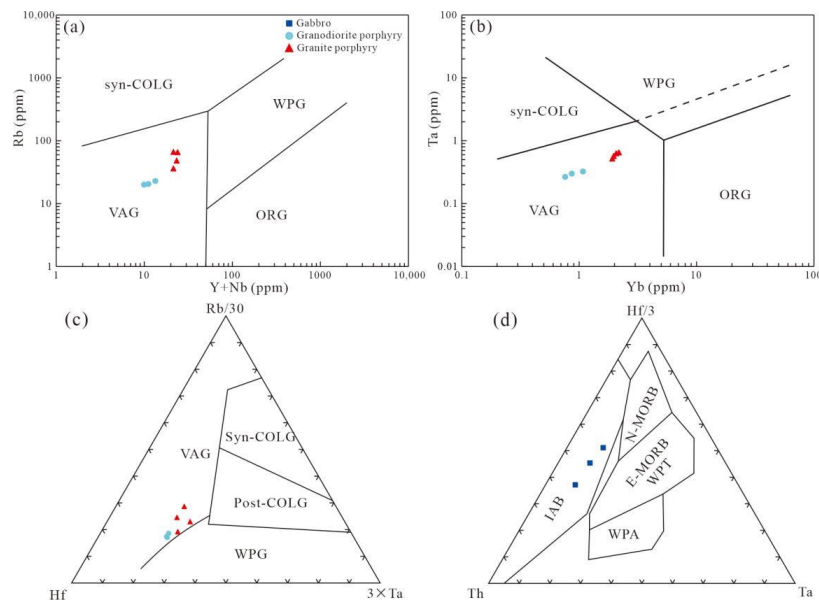


Figure 14. (a) Rb vs. (Y+Nb) diagram [113], (b) Ta vs. Yb diagram [113], and (c) Rb/30-Hf-3×Ta diagram [114] for the granitic rocks. WPG, within-plate granites; VAG, volcanic arc granites; Syn-COLG, syn-collision granites; Post-COLG, post-collision granites; ORG, ocean ridge granites. (d) Hf/3-Th-Ta diagram [111] for the gabbro. IAB, island arc basalt; N-MORB, normal-type mid-ocean ridge basalt; E-MORB, enriched-type mid-ocean ridge basalt; WPA, within-plate alkalic; WPT, within-plate tholeiite.

As discussed above, the partial melting of the Kangguer oceanic slab produced parental magmas of the plagiogranite porphyry (335–332 Ma, [5,22,23]), granodiorite porphyry (321.8 ± 3.1 Ma, this study), and, possibly, Chihu porphyritic granodiorite (314.5 ± 2.5 Ma, [14]). Since normal subduction zones have lower temperatures than the adjacent mantle, it is generally believed that the partial melting of the subducting slab cannot occur, but rather dehydration leads to the partial melting of the overlying mantle wedge [115], with the formation of arc-related calc-alkaline basaltic-andesitic-dacitic-rhyolitic igneous rocks [116]. Therefore, the existence of adakites derived from the partial melting of the subducting slab may indicate a special environment. Adakites are originally thought to be associated with the subduction of the young (≤ 25 Ma) and hot oceanic lithosphere [52]. Other studies revealed that adakitic rocks can be formed in various tectonic settings as long as a high geothermal gradient exists [105], such as the initial subduction of an old crust [117], ridge subduction [118], flat subduction [119], or post-collision [116]. Combined with regional sedimentation, magmatism, and tectonism, the subduction of the young and hot oceanic lithosphere, initial subduction of an old crust, and post-collision setting during the Early Late Carboniferous (335–315 Ma) seem unlikely. In addition to adakites, ridge subduction usually produces high-Mg andesites and Nb-enriched basalts ($Nb > 20$ ppm) [120]. The reported basalts and the studied gabbro that are temporally and spatially close to the adakitic rocks in the Tuwu-Yandong belt have low Nb contents (almost all < 10 ppm, and mostly < 5 ppm; see Supplementary Table S1), ruling out ridge subduction. As an unusual mode of subduction, flat subduction, which occurs in ca. 10% of the world's convergent margins, can produce the temperature and pressure conditions necessary for the fusion of a moderately old oceanic crust [105]. The upper part and leading edge of the slab can melt during the early stages of flat subduction [119]. Hence, we speculate the formation of the adakites in the Tuwu-Yandong belt was most likely caused by the northward flat subduction of the Kangguer Ocean. This is further supported by the increasing Ce/Y ratios of the basic rocks and Ho/Yb ratios of the felsic rocks (from the latest part of the Early Carboniferous to the Late Carboniferous) in the Dananhu and Bogeda belt, indicating significant crustal thickening, which is likely associated with high- to low-angle subduction transition [25]. Furthermore, prolonged flat subduction both cools the lithospheres and impedes the partial melting of the subducting oceanic crust [119], which may be consistent with the gradually weakening adakitic features (e.g., the decreasing Sr/Y ratio and increasing Y content of the adakites) from Early Carboniferous to Late Carboniferous (335–315 Ma) in the Tuwu-Yandong belt (Figure 6a; [5,14] and references therein; this study).

As flat subduction continues, the gradually cooling subducting slab phases into the eclogite facies, with the gravity increasing, which leads the subducting slab to become increasingly unstable [121], possibly transforming into a higher-angle subduction. The rollback (or low- to high-angle subduction transition) of the subducted slab causes the strong upwelling of the asthenosphere, provoking strong asthenosphere-lithosphere interactions and the partial melting of juvenile lower crust [10]. Some magmatism and mineralization data indicate that slab rollback may have occurred in the Dananhu island arc in the Late Carboniferous (ca. 314 Ma), such as (1) the high-Al gabbro (313.5 ± 1.2 Ma) and non-fractionated I-type granite porphyry (309.8 ± 2.5 Ma) in the Tuwu-Yandong belt, of which the latter is considered to be derived from the partial melting of the juvenile lower crust under garnet-free amphibolite facies conditions (this study), and (2) the Haibaotan gabbro (315.5 ± 1.9 Ma), associated with magmatic Cu-Ni mineralization along the Dacaotan fault, which is thought to have formed in a subduction setting [122]. The inference of slab rollback is reinforced by the ca. 311 Ma K-feldspar granites (located approximately 30 km northeast of the Chihu deposit) showing variable Nb/La ratios (0.38–1.07) ($Nb/La < 0.71$ for the rocks formed in subduction settings, $Nb/La > 0.71$ for the rocks in a lithospheric extension or mantle plume environments [95,123]), indicating that they were formed by subduction-related materials with a significant addition of intraplate components [61]. No younger magmatism after 310 Ma has been identified in the Tuwu-Yandong belt, which

may indicate a “quiet period” before the final closure of the ancient Tianshan Ocean along the Kangguer Fault in the belt [10].

Based on the above discussion, we propose a new Carboniferous tectono-magmatic-metallogenetic evolution model of the Tuwu-Yandong porphyry Cu belt (Figure 15). At ca. 335–315 Ma, the flat subduction induced the partial melting of the subducted slab [10], producing the adakitic rocks (e.g., plagiogranite porphyry, granodiorite porphyry, and Chihu porphyritic granodiorite) and associated porphyry Cu mineralization (e.g., Fuxing, Yandong, Tuwu, Linglong, and Chihu, [15]) (Figure 15a). At ca. 314–310 Ma, slab rollback induced (a) the partial melting of the subduction-modified and depleted mantle wedge, producing the high-Al gabbro, and (b) the partial melting of the juvenile lower crust, producing the non-fractionated I-type granite porphyry and K-feldspar granites with a significant addition of intraplate components [67] (Figure 15b).

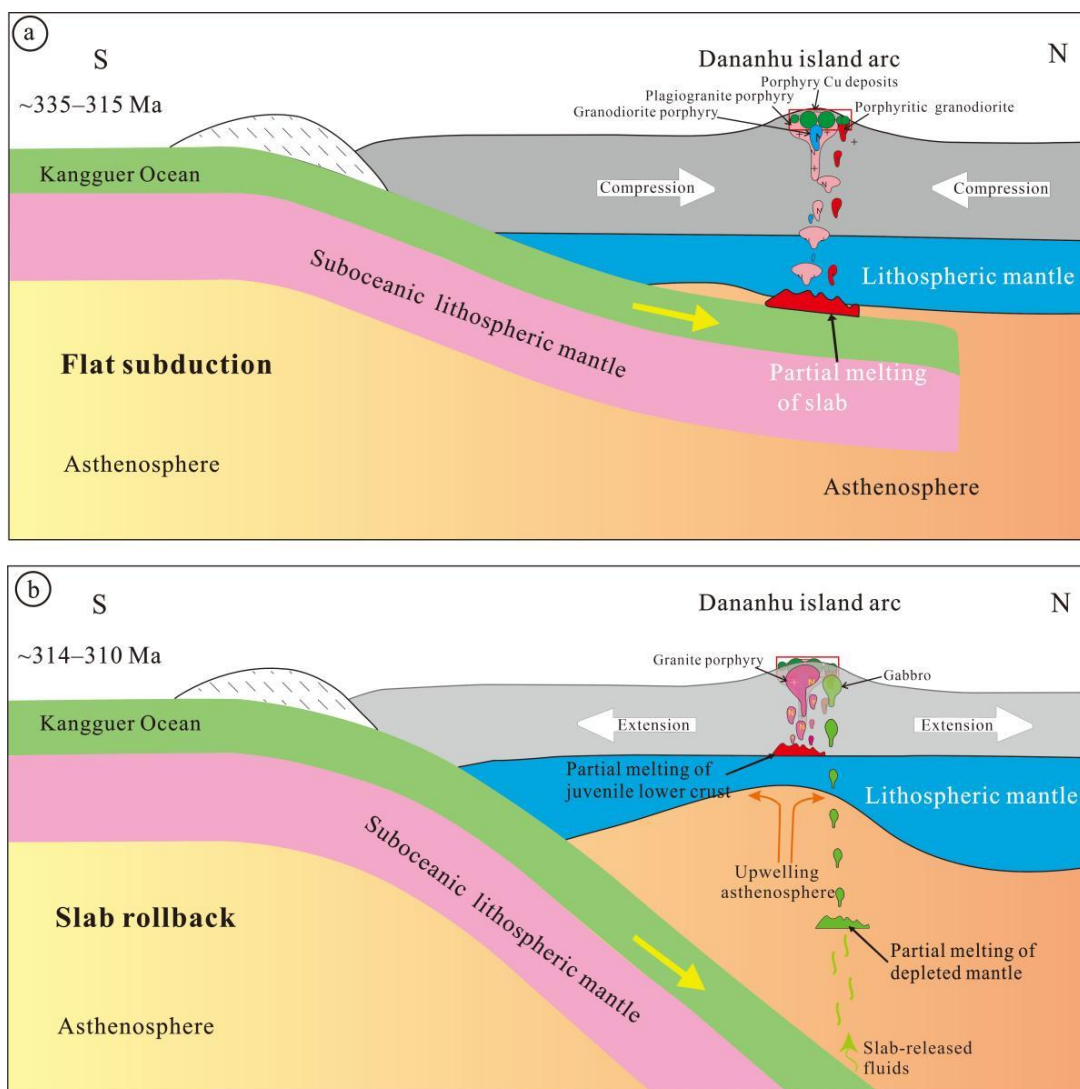


Figure 15. Schematic cartoons illustrating the Carboniferous tectono-magmatic-metallogenetic evolution model of the Tuwu-Yandong porphyry Cu belt in eastern Tianshan. (a) The northward flat subduction of the Kangguer ocean slab induced the partial melting of the subducted slab, producing the adakitic rocks and associated porphyry Cu mineralization during ca. 335–315 Ma. (b) The ca. 314–310 Ma slab rollback induced the partial melting of the subduction-modified and depleted mantle and juvenile lower crust, producing high-Al gabbro and non-fractionated I-type granite porphyry, respectively.

6. Conclusions

- (1) New LA-ICP-MS zircon U-Pb geochronology indicates that the granodiorite porphyry, gabbro, and granite porphyry were emplaced at 321.8 ± 3.1 Ma, 313.5 ± 1.2 Ma and 309.8 ± 2.5 Ma, respectively.
- (2) The zircon trace elements of the Carboniferous intrusions in the Tuwu-Yandong belt imply that the granodiorite porphyry is likely derived from a more oxidized and hydrous magma source than that of the gabbro and granite porphyry, which may favor the formation of porphyry Cu deposits.
- (3) The adakitic granodiorite porphyry is derived from the partial melting of the subducted oceanic slab, with subsequent interactions with mantle peridotite. The high-Al gabbro is derived from the partial melting of a depleted mantle wedge hydrated by slab-released fluids, while the non-fractionated I-type granite porphyry is derived from the partial melting of the juvenile lower crust.
- (4) The northward flat subduction of the Kangguer ocean slab at ca. 335–315 Ma facilitated the formation of the adakites and associated porphyry Cu mineralization in the Tuwu-Yandong belt. After the prolonged flat subduction, slab rollback may have occurred at ca. 314–310 Ma.

Supplementary Materials: The following supporting information can be downloaded at: <https://www.mdpi.com/article/10.3390/min12121573/s1>, Tables S1–S3. Table S1: Published whole-rock major (in wt%) and trace element (in ppm) compositions for Carboniferous magmatic rocks in the Tuwu-Yandong belt (and adjacent areas in the middle section of the Dananhu island arc). Table S2: Published in-situ zircon Lu-Hf isotope compositions for Carboniferous magmatic rocks in the Tuwu-Yandong belt (and adjacent areas in the middle section of the Dananhu island arc). Table S3: Published Sr-Nd isotopic compositions of Carboniferous magmatic rocks in the Tuwu-Yandong belt (and adjacent areas in the middle section of the Dananhu island arc).

Author Contributions: Conceptualization, W.A. and C.X.; investigation, W.A., Y.Z., D.X., B.C. and C.X.; methodology, W.A., C.L. and C.X.; data curation, W.A. and C.L.; writing—original draft preparation, W.A.; writing—review and editing, W.A., Y.Z. and C.X.; supervision, C.X.; funding acquisition, C.X., C.L. and Y.Z. All authors have read and agreed to the published version of the manuscript.

Funding: This research was jointly funded by the National Key R&D Program of China (2020YFA0714800 and 2017YFC0601202), the National Natural Science Foundation of China (41873065, 41803013, and 41473017), the Open Research Project from the State Key Laboratory of Geological Processes and Mineral Resources (GPMR202107, GPMR202116), the Open Funds from the Key Laboratory of Deep Earth Dynamics of Ministry of Natural Resource (J1901-16), the State Key Laboratory for Mineral Deposits Research (2021-LAMD-K10), and Fundamental Research Funds for the Central Universities (QZ05201905 and 2652019050).

Data Availability Statement: All the data are presented in the paper.

Acknowledgments: The authors would like to thank the managers and geological staff of No. 1 Geological Team of Xinjiang for their support with the fieldwork. The authors are also deeply grateful for the reviews and constructive suggestions of the anonymous reviewers.

Conflicts of Interest: The authors declare no conflict of interest.

References

1. Windley, B.F.; Alexeiev, D.; Xiao, W.; Kröner, A.; Badarch, G. Tectonic models for accretion of the Central Asian Orogenic Belt. *J. Geol. Soc.* **2007**, *164*, 31–47. [[CrossRef](#)]
2. Gao, J.; Klemd, R.; Zhu, M.; Wang, X.-S.; Li, J.; Wan, B.; Xiao, W.; Zeng, Q.; Shen, P.; Sun, J.; et al. Large-scale porphyry-type mineralization in the Central Asian metallogenic domain: A review. *J. Asian Earth Sci.* **2018**, *165*, 7–36. [[CrossRef](#)]
3. Shen, P.; Hattori, K.; Pan, H.; Jackson, S.; Seitmuratova, E. Oxidation condition and metal fertility of granitic magmas: Zircon trace-element data from porphyry Cu deposits in the Central Asian orogenic belt. *Econ. Geol.* **2015**, *110*, 1861–1878. [[CrossRef](#)]
4. Wang, Y.-H.; Zhang, F.-F.; Xue, C.-J.; Liu, J.-J.; Zhang, Z.-C.; Sun, M. Geology and Genesis of the Tuwu Porphyry Cu Deposit, Xinjiang, Northwest China. *Econ. Geol.* **2021**, *116*, 471–500. [[CrossRef](#)]

5. Wang, Y.-H.; Xue, C.-J.; Liu, J.-J.; Zhang, F.-F. Origin of the subduction-related Carboniferous intrusions associated with the Yandong porphyry Cu deposit in eastern Tianshan, NW China: Constraints from geology, geochronology, geochemistry, and Sr–Nd–Pb–Hf–O isotopes. *Miner. Depos.* **2017**, *53*, 629–647. [[CrossRef](#)]
6. Zhao, Y.; Xue, C.; Liu, S.-A.; Mathur, R.; Zhao, X.; Yang, Y.; Dai, J.; Man, R.; Liu, X. Redox reactions control Cu and Fe isotope fractionation in a magmatic Ni–Cu mineralization system. *Geochim. Cosmochim. Acta* **2019**, *249*, 42–58. [[CrossRef](#)]
7. Sun, Y.; Wang, J.; Li, Y.; Wang, Y.; Yu, M.; Long, L.; Lü, X.; Chen, L. Recognition of Late Ordovician Yudai porphyry Cu (Au, Mo) mineralization in the Kalatag district, Eastern Tianshan terrane, NW China: Constraints from geology, geochronology, and petrology. *Ore Geol. Rev.* **2018**, *100*, 220–236. [[CrossRef](#)]
8. Zhang, F.-F.; Wang, Y.-H.; Liu, J.-J.; Xue, C.-J.; Wang, J.-P.; Zhang, W.; Li, Y.-Y. Paleozoic Magmatism and Mineralization Potential of the Sanchakou Copper Deposit, Eastern Tianshan, Northwest China: Insights from Geochronology, Mineral Chemistry, and Isotopes. *Econ. Geol.* **2022**, *117*, 165–194. [[CrossRef](#)]
9. Wang, Y.; Zhang, F.; Liu, J. The genesis of the ores and intrusions at the Yuhai Cu–Mo deposit in eastern Tianshan, NW China: Constraints from geology, geochronology, geochemistry, and Hf isotope systematics. *Ore Geol. Rev.* **2016**, *77*, 312–331. [[CrossRef](#)]
10. Xiao, B.; Chen, H.; Hollings, P.; Han, J.; Wang, Y.; Yang, J.; Cai, K. Magmatic evolution of the Tuwu–Yandong porphyry Cu belt, NW China: Constraints from geochronology, geochemistry and Sr–Nd–Hf isotopes. *Gondwana Res.* **2017**, *43*, 74–91. [[CrossRef](#)]
11. Wang, Y.H.; Zhang, F.F.; Liu, J.J.; Que, C.Y. Genesis of the Fuxing porphyry Cu deposit in Eastern Tianshan, China: Evidence from fluid inclusions and C–H–O–S–Pb isotope systematics. *Ore Geol. Rev.* **2016**, *79*, 46–61. [[CrossRef](#)]
12. Wang, Y.-H.; Zhang, F.-F.; Li, B.-C. Genesis of the Yandong porphyry Cu deposit in eastern Tianshan, NW China: Evidence from geology, fluid inclusions and isotope systematics. *Ore Geol. Rev.* **2017**, *86*, 280–296. [[CrossRef](#)]
13. Sun, M.; Wang, Y.-H.; Zhang, F.-F.; Lin, S.-Y.; Xue, C.-J.; Liu, J.-J.; Zhu, D.-C.; Wang, K.; Zhang, W. Petrogenesis of Late Carboniferous intrusions in the Linglong area of Eastern Tianshan, NW China, and tectonic implications: Geochronological, geochemical, and zircon Hf–O isotopic constraints. *Ore Geol. Rev.* **2020**, *120*, 103462. [[CrossRef](#)]
14. Zhang, F.; Wang, Y.; Liu, J. Petrogenesis of Late Carboniferous granitoids in the Chihu area of Eastern Tianshan, Northwest China, and tectonic implications: Geochronological, geochemical, and zircon Hf–O isotopic constraints. *Int. Geol. Rev.* **2016**, *58*, 949–966. [[CrossRef](#)]
15. An, W.; Xue, C.; Zhao, Y.; Li, C. Two Periods of Porphyry Cu Mineralization and Metallogenetic Implications in the Tuwu–Yandong Belt (NW China), Based on Re–Os Systematics of Molybdenite. *Minerals* **2022**, *12*, 1127. [[CrossRef](#)]
16. Wang, Y.; Chen, H.; Baker, M.J.; Han, J.; Xiao, B.; Yang, J.; Jourdan, F. Multiple mineralization events of the Paleozoic Tuwu porphyry copper deposit, Eastern Tianshan: Evidence from geology, fluid inclusions, sulfur isotopes, and geochronology. *Miner. Depos.* **2018**, *54*, 1053–1076. [[CrossRef](#)]
17. Wang, Y.; Chen, H.; Xiao, B.; Han, J.; Fang, J.; Yang, J.; Jourdan, F. Overprinting mineralization in the Paleozoic Yandong porphyry copper deposit, Eastern Tianshan, NW China—Evidence from geology, fluid inclusions and geochronology. *Ore Geol. Rev.* **2018**, *100*, 148–167. [[CrossRef](#)]
18. Xiao, B.; Chen, H.; Wang, Y.; Han, J.; Xu, C.; Yang, J. Chlorite and epidote chemistry of the Yandong Cu deposit, NW China: Metallogenetic and exploration implications for Paleozoic porphyry Cu systems in the Eastern Tianshan. *Ore Geol. Rev.* **2018**, *100*, 168–182. [[CrossRef](#)]
19. Shen, P.; Pan, H.; Dong, L. Yandong porphyry Cu deposit, Xinjiang, China—Geology, geochemistry and SIMS U–Pb zircon geochronology of host porphyries and associated alteration and mineralization. *J. Asian Earth Sci.* **2014**, *80*, 197–217. [[CrossRef](#)]
20. Shen, P.; Pan, H.; Zhou, T.; Wang, J. Petrography, geochemistry and geochronology of the host porphyries and associated alteration at the Tuwu Cu deposit, NW China: A case for increased depositional efficiency by reaction with mafic hostrock? *Miner. Depos.* **2014**, *49*, 709–731. [[CrossRef](#)]
21. Wang, Y.-H.; Zhang, F.-F.; Liu, J.-J.; Que, C.-Y. Carboniferous magmatism and mineralization in the area of the Fuxing Cu deposit, Eastern Tianshan, China: Evidence from zircon U–Pb ages, petrogeochemistry, and Sr–Nd–Hf–O isotopic compositions. *Gondwana Res.* **2016**, *34*, 109–128. [[CrossRef](#)]
22. Wang, Y.-H.; Xue, C.-J.; Liu, J.-J.; Wang, J.-P.; Yang, J.-T.; Zhang, F.-F.; Zhao, Z.-N.; Zhao, Y.-J.; Liu, B. Early Carboniferous adakitic rocks in the area of the Tuwu deposit, eastern Tianshan, NW China: Slab melting and implications for porphyry copper mineralization. *J. Southeast Asian Earth Sci.* **2015**, *103*, 332–349. [[CrossRef](#)]
23. Zhang, L.; Xiao, W.; Qin, K.; Zhang, Q. The adakite connection of the Tuwu–Yandong copper porphyry belt, eastern Tianshan, NW China: Trace element and Sr–Nd–Pb isotope geochemistry. *Miner. Depos.* **2006**, *41*, 188–200. [[CrossRef](#)]
24. Xia, L.-Q.; Xu, X.-Y.; Xia, Z.-C.; Li, X.-M.; Ma, Z.-P.; Wang, L.-S. Petrogenesis of Carboniferous rift-related volcanic rocks in the Tianshan, northwestern China. *GSA Bull.* **2004**, *116*, 419–433. [[CrossRef](#)]
25. Zhang, Y.; Sun, M.; Yuan, C.; Long, X.; Jiang, Y.; Li, P.; Huang, Z.; Du, L. Alternating Trench Advance and Retreat: Insights From Paleozoic Magmatism in the Eastern Tianshan, Central Asian Orogenic Belt. *Tectonics* **2018**, *37*, 2142–2164. [[CrossRef](#)]
26. TF, Z.; DY, Z.; MX, P.; JD, Z. Geochronology, tectonic setting and mineralization of granitoids in Jueluotage area, eastern Tianshan, Xinjiang. *Acta Petrol. Sin.* **2010**, *26*, 478–502.
27. Zhang, D.; Zhou, T.; Yuan, F.; Fiorentini, M.L.; Said, N.; Lu, Y.; Pirajno, F. Geochemical and isotopic constraints on the genesis of the Jueluotage native copper mineralized basalt, Eastern Tianshan, Northwest China. *J. Southeast Asian Earth Sci.* **2013**, *73*, 317–333. [[CrossRef](#)]

28. Chen, L.; Wang, J.-B.; Bagas, L.; Wu, X.-B.; Zou, H.-Y.; Zhang, H.-Q.; Sun, Y.; Lv, X.-Q.; Deng, X.-H. Significance of adakites in petrogenesis of early Silurian magmatism at the Yudai copper deposit in the Kalatag district, NW China. *Ore Geol. Rev.* **2017**, *91*, 780–794. [[CrossRef](#)]
29. Xiao, W.; Windley, B.F.; Allen, M.B.; Han, C. Paleozoic multiple accretionary and collisional tectonics of the Chinese Tianshan orogenic collage. *Gondwana Res.* **2013**, *23*, 1316–1341. [[CrossRef](#)]
30. Gao, R.; Xue, C.; Chi, G.; Dai, J.; Dong, C.; Zhao, X.; Man, R. Genesis of the giant Caixiasan Zn-Pb deposit in Eastern Tianshan, NW China: Constraints from geology, geochronology and S-Pb isotopic geochemistry. *Ore Geol. Rev.* **2020**, *119*, 103366. [[CrossRef](#)]
31. Sun, Y.; Wang, J.; Wang, Y.; Long, L.; Mao, Q.; Yu, M. Ages and origins of granitoids from the Kalatag Cu cluster in Eastern Tianshan, NW China: Constraints on Ordovician–Devonian arc evolution and porphyry Cu fertility in the Southern Central Asian orogenic belt. *Lithos* **2019**, *330–331*, 55–73. [[CrossRef](#)]
32. Deng, X.-H.; Wang, J.-B.; Pirajno, F.; Mao, Q.-G.; Long, L.-L. A review of Cu-dominant mineral systems in the Kalatag district, East Tianshan, China. *Ore Geol. Rev.* **2019**, *117*, 103284. [[CrossRef](#)]
33. Wang, Y.-H.; Xue, C.-J.; Gao, J.-B.; Zhang, F.-F.; Liu, J.-J.; Wang, J.-P.; Wang, J.-C. The genesis of the ores and granitic rocks at the Hongshi Au deposit in Eastern Tianshan, China: Constraints from zircon U-Pb geochronology, geochemistry and isotope systematics. *Ore Geol. Rev.* **2016**, *74*, 122–138. [[CrossRef](#)]
34. Wang, Y.H.; Zhang, F.F.; Liu, J.J.; Xue, C.J.; Li, B.C.; Xian, X.C. Ore Genesis and Hydrothermal Evolution of the Donggebi Porphyry Mo Deposit, Xinjiang, Northwest China: Evidence from Isotopes (C, H, O, S, Pb), Fluid Inclusions, and Molybdenite Re-Os Dating. *Econ. Geol.* **2018**, *113*, 463–488. [[CrossRef](#)]
35. Sun, H.; Li, H.; Danišík, M.; Xia, Q.; Jiang, C.; Wu, P.; Yang, H.; Fan, Q.; Zhu, D. U-Pb and Re-Os geochronology and geochemistry of the Donggebi Mo deposit, Eastern Tianshan, NW China: Insights into mineralization and tectonic setting. *Ore Geol. Rev.* **2017**, *86*, 584–599. [[CrossRef](#)]
36. Zhao, Y.; Xue, C.; Symons, D.T.; Zhao, X.; Zhang, G.; Yang, Y.; Zu, B. Temporal variations in the mantle source beneath the Eastern Tianshan nickel belt and implications for Ni-Cu mineralization potential. *Lithos* **2018**, *314*, 597–616. [[CrossRef](#)]
37. Zhang, S.; Chen, H.; Hollings, P.; Zhao, L.; Gong, L. Tectonic and magmatic evolution of the Aqishan-Yamansu belt: A Paleozoic arc-related basin in the Eastern Tianshan (NW China). *GSA Bull.* **2020**, *133*, 1320–1344. [[CrossRef](#)]
38. Hou, G.S.; Tang, H.F.; Liu, C.Q.; Wang, Y.B. Geochronological and geochemical study on the wallrock of Tuwu-Yandong porphyry copper deposits, eastern Tianshan mountains. *Acta Petrol. Sin.* **2005**, *21*, 1729–1736.
39. Mao, Q.; Xiao, W.; Ao, S.; Li, R.; Wang, H.; Tan, Z.; Tan, W. Late Devonian to early Carboniferous roll-back related extension setting for the Tuwu-Yandong porphyry copper metallogenic belt in the Dananhu arc of the eastern Tianshan (NW China) in the southern Altaids. *Ore Geol. Rev.* **2022**, *149*, 105060. [[CrossRef](#)]
40. Liu, Y.; Hu, Z.; Zong, K.; Gao, C.; Gao, S.; Xu, J.; Chen, H. Reappraisal and refinement of zircon U-Pb isotope and trace element analyses by LA-ICP-MS. *Chin. Sci. Bull.* **2010**, *55*, 1535–1546. [[CrossRef](#)]
41. Ludwig, K.R. *Isoplot/Ex, Version 3: A Geochronological Toolkit for Microsoft Excel*; Berkley; Berkeley Geochronology Center: Berkeley, CA, USA, 2003.
42. Ballard, R.J.; Palin, M.J.; Campbell, I.H. Relative oxidation states of magmas inferred from Ce (IV)/Ce (III) in zircon: Application to porphyry copper deposits of northern Chile. *Contrib. Mineral. Petrol.* **2002**, *144*, 347–364. [[CrossRef](#)]
43. Elhlou, S.; Belousova, E.; Griffin, W.; Pearson, N.; O'Reilly, S. Trace element and isotopic composition of GJ-red zircon standard by laser ablation. *Geochim. Cosmochim. Acta* **2006**, *70*, A158. [[CrossRef](#)]
44. Tang, G.-J.; Wang, Q.; Wyman, D.A.; Li, Z.-X.; Zhao, Z.-H.; Yang, Y.-H. Late Carboniferous high ϵ Nd(t)– ϵ Hf(t) granitoids, enclaves and dikes in western Junggar, NW China: Ridge-subduction-related magmatism and crustal growth. *Lithos* **2012**, *140–141*, 86–102. [[CrossRef](#)]
45. Liang, Q.; Jing, H.; Gregoire, D.C. Determination of trace elements in granites by inductively coupled plasma mass spectrometry. *Talanta* **2000**, *51*, 507–513. [[CrossRef](#)] [[PubMed](#)]
46. Rickwood, P.C. Boundary lines within petrologic diagrams which use oxides of major and minor elements. *Lithos* **1989**, *22*, 247–263. [[CrossRef](#)]
47. Rollinson, H.; Pease, V. *Using Geochemical Data: To Understand Geological Processes*, 2nd ed.; Cambridge University Press: Cambridge, UK, 2021.
48. Irvine, T.N.; Baragar, W.R.A. A Guide to the Chemical Classification of the Common Volcanic Rocks. *Can. J. Earth Sci.* **1971**, *8*, 523–548. [[CrossRef](#)]
49. Maniar, D.P.; Piccoli, P.M. Tectonic discrimination of granitoids. *Geol. Soc. Am. Bull.* **1989**, *101*, 635–643. [[CrossRef](#)]
50. Boynton, W.V. Chapter 3—Cosmochemistry of the Rare Earth Elements: Meteorite Studies. In *Developments in Geochemistry*; Henderson, P., Ed.; Elsevier: Amsterdam, The Netherlands, 1984; pp. 63–114.
51. Sun, S.S.; McDonough, W.F. Chemical and isotopic systematics of oceanic basalts: Implications for mantle composition and processes. In *Magmatism in the Ocean Basin*; Geological Society Special Publication: London, UK, 1989; Volume 42, pp. 313–345.
52. Defant, M.J.; Drummond, M.S. Derivation of some modern arc magmas by melting of young subducted lithosphere. *Nature* **1990**, *347*, 662–665. [[CrossRef](#)]
53. Hoskin, P.W.O.; Schaltegger, U. The composition of zircon and igneous and metamorphic petrogenesis. *Rev. Mineral. Geochem.* **2003**, *53*, 27–62. [[CrossRef](#)]

54. Wang, T.-G.; Li, H.; Liu, J.-S.; Evans, N.J.; Wang, Y.-C.; Zha, D. Whole-rock and zircon geochemistry of the Xiaoliugou granites, North Qilian Orogen (NW China): Implications for tectonic setting, magma evolution and W–Mo mineralization. *Ore Geol. Rev.* **2019**, *115*, 103166. [[CrossRef](#)]
55. Watson, E.B.; Wark, D.A.; Thomas, J.B. Crystallization thermometers for zircon and rutile. *Contrib. Mineral. Petrol.* **2006**, *151*, 413–433. [[CrossRef](#)]
56. McDonough, W.F.; Sun, S. The composition of the Earth. *Chem. Geol.* **1995**, *120*, 223–253. [[CrossRef](#)]
57. Ferry, J.M.; Watson, E.B. New thermodynamic models and revised calibrations for the Ti-in-zircon and Zr-in-rutile thermometers. *Contrib. Mineral. Petrol.* **2007**, *154*, 429–437. [[CrossRef](#)]
58. Trail, D.; Watson, E.B.; Tailby, N.D. Ce and Eu anomalies in zircon as proxies for the oxidation state of magmas. *Geochim. Cosmochim. Acta* **2012**, *97*, 70–87. [[CrossRef](#)]
59. Blichert-Toft, J.; Albarède, F. The Lu-Hf isotope geochemistry of chondrites and the evolution of the mantle-crust system. *Earth Planet. Sci. Lett.* **1997**, *148*, 243–258. [[CrossRef](#)]
60. Griffin, W.L.; Pearson, N.J.; Belousova, E.; Jackson, S.V.; Van Achterbergh, E.; O'Reilly, S.Y.; Shee, S.R. The Hf isotope composition of cratonic mantle: LAM-MC-ICPMS analysis of zircon megacrysts in kimberlites. *Geochim. Cosmochim. Acta* **2000**, *64*, 133–147. [[CrossRef](#)]
61. Söderlund, U.; Patchett, P.J.; Vervoort, J.D.; Isachsen, C.E. The ^{176}Lu decay constant determined by Lu–Hf and U–Pb isotope systematics of Precambrian mafic intrusions. *Earth Planet. Sci. Lett.* **2004**, *219*, 311–324. [[CrossRef](#)]
62. Qiu, K.F.; Taylor, R.D.; Song, Y.H.; Yu, H.C.; Song, K.R.; Li, N. Geologic and geochemical insights into the formation of the Taiyangshan porphyry copper–molybdenum deposit, Western Qinling Orogenic Belt, China. *Gondwana Res.* **2016**, *35*, 40–58. [[CrossRef](#)]
63. Qiu, K.-F.; Deng, J. Petrogenesis of granitoids in the Dewulu skarn copper deposit: Implications for the evolution of the Paleotethys ocean and mineralization in Western Qinling, China. *Ore Geol. Rev.* **2017**, *90*, 1078–1098. [[CrossRef](#)]
64. Chen, F.W.; Li, H.Q.; Chen, Y.C.; Wang, D.H.; Wang, J.L.; Liu, D.Q.; Zhou, R.H. Zircon SHRIMP U–Pb dating and its geological significance of mineralization in Tuwu-Yandong porphyry copper mine, East Tianshan Mountain. *Acta Geol. Sin.* **2005**, *79*, 256–261.
65. Wang, Y.; Xue, C.; Wang, J.; Peng, R.; Yang, J.; Zhang, F.; Zhao, Z.; Zhao, Y. Petrogenesis of magmatism in the Yandong region of Eastern Tianshan, Xinjiang: Geochemical, geochronological, and Hf isotope constraints. *Int. Geol. Rev.* **2014**, *57*, 1130–1151. [[CrossRef](#)]
66. Wu, H.; Li, H.Q.; Chen, F.W.; Lu, Y.F.D.; Mei, Y.P. Zircon SHRIMP U–Pb dating of plagiogranite porphyry in the Chihu molybdenum-copper district, Hami, East Tianshan. *Geol. Bull. China* **2006**, *25*, 549–552.
67. Du, L.; Yuan, C.; Li, X.-P.; Zhang, Y.; Huang, Z.; Long, X. Petrogenesis and Geodynamic Implications of the Carboniferous Granitoids in the Dananhu Belt, Eastern Tianshan Orogenic Belt. *J. Earth Sci.* **2019**, *30*, 1243–1252. [[CrossRef](#)]
68. Rui, Z.Y. Discussion on metallogenic epoch of Tuwu and Yandong porphyry copper deposits in eastern Tianshan Mountains, Xinjiang. *Miner. Depos.* **2002**, *21*, 16–22.
69. Zhang, L.; Qin, K.; Xiao, W. Multiple mineralization events in the eastern Tianshan district, NW China: Isotopic geochronology and geological significance. *J. Southeast Asian Earth Sci.* **2008**, *32*, 236–246. [[CrossRef](#)]
70. Dayu, Z.; Taofa, Z.; Feng, Y.; Yu, F.; Shuai, L.; MingXing, P. Geochemical characters, metallogenic chronology and geological significance of the Yanxi copper deposit in eastern Tianshan, Xinjiang. *Acta Petrol. Sin.* **2010**, *26*, 3327–3338.
71. Mao, Q.; Ao, S.; Song, D.; Xiao, W.; Windley, B.F.; Sang, M.; Tan, Z.; Wang, H.; Li, R. Silurian to early Permian slab melting and crustal growth in the southern Altaids: Insights from adakites and associated mineral deposits in the Dananhu arc, Eastern Tianshan, NW China. *Geol. Rundsch.* **2021**, *110*, 2115–2131. [[CrossRef](#)]
72. Wang, Y.; Xue, C.; Liu, J.; Wang, J.; Yang, J.; Zhang, F.; Zhao, Z.; Zhao, Y. Geochemistry, geochronology, Hf isotope, and geological significance of the Tuwu porphyry copper deposit in eastern Tianshan, Xinjiang. *Acta Petrol. Sin.* **2014**, *30*, 3383–3399.
73. Wang, R.; Richards, J.P.; Hou, Z.-Q.; Yang, Z.; Gou, Z.-B.; Dufrane, S.A. Increasing Magmatic Oxidation State from Paleocene to Miocene in the Eastern Gangdese Belt, Tibet: Implication for Collision-Related Porphyry Cu–Mo Au Mineralization. *Econ. Geol.* **2014**, *109*, 1943–1965. [[CrossRef](#)]
74. Sun, W.; Huang, R.-F.; Li, H.; Hu, Y.-B.; Zhang, C.-C.; Sun, S.-J.; Zhang, L.-P.; Ding, X.; Li, C.-Y.; Zartman, R.E.; et al. Porphyry deposits and oxidized magmas. *Ore Geol. Rev.* **2014**, *65*, 97–131. [[CrossRef](#)]
75. Shu, Q.; Chang, Z.; Lai, Y.; Hu, X.; Wu, H.; Zhang, Y.; Wang, P.; Zhai, D.; Zhang, C. Zircon trace elements and magma fertility: Insights from porphyry (-skarn) Mo deposits in NE China. *Miner. Depos.* **2019**, *54*, 645–656. [[CrossRef](#)]
76. Liang, H.; Campbell, I.H.; Allen, C.; Sun, W.; Liu, C.; Yu, H.; Xie, Y.; Zhang, Y. Zircon Ce⁴⁺/Ce³⁺ ratios and ages for Yulong ore-bearing porphyries in eastern Tibet. *Miner. Depos.* **2006**, *41*, 152–159. [[CrossRef](#)]
77. Xin, H.B.; Qu, X.M. Relative oxidation states of ore-bearing porphyries inferred from Ce (IV)/Ce (III) ratio in zircon: Application to the porphyry copper belt at Gangdese, Tibet. *Acta Mineral. Sin.* **2008**, *28*, 152–160.
78. Han, Y.; Zhang, S.; Pirajno, F.; Zhou, X.; Zhao, G.; Qü, W.; Liu, S.; Zhang, J.; Liang, H.; Yang, K. U–Pb and Re–Os isotopic systematics and zircon Ce⁴⁺/Ce³⁺ ratios in the Shiyaogou Mo deposit in eastern Qinling, central China: Insights into the oxidation state of granitoids and Mo (Au) mineralization. *Ore Geol. Rev.* **2013**, *55*, 29–47. [[CrossRef](#)]
79. Wang, Y.; Chen, H.; Han, J.; Chen, S.; Huang, B.; Li, C.; Tian, Q.; Wang, C.; Wu, J.; Chen, M. Paleozoic tectonic evolution of the Dananhu-Tousuquan island arc belt, Eastern Tianshan: Constraints from the magmatism of the Yuhai porphyry Cu deposit, Xinjiang, NW China. *J. Southeast Asian Earth Sci.* **2018**, *153*, 282–306. [[CrossRef](#)]

80. Trail, D.; Watson, E.B.; Tailby, N.D. The oxidation state of Hadean magmas and implications for early Earth's atmosphere. *Nature* **2011**, *480*, 79–82. [[CrossRef](#)]
81. Sun, W.; Zhang, H.; Ling, M.-X.; Ding, X.; Chung, S.-L.; Zhou, J.; Yang, X.-Y.; Fan, W. The genetic association of adakites and Cu–Au ore deposits. *Int. Geol. Rev.* **2010**, *53*, 691–703. [[CrossRef](#)]
82. Hou, Z.; Pan, X.; Li, Q.; Yang, Z.; Song, Y. The giant Dexing porphyry Cu–Mo–Au deposit in east China: Product of melting of juvenile lower crust in an intracontinental setting. *Miner. Depos.* **2013**, *48*, 1019–1045. [[CrossRef](#)]
83. Guo, F.; Fan, W.; Wang, Y.; Zhang, M. Origin of early Cretaceous calc-alkaline lamprophyres from the Sulu orogen in eastern China: Implications for enrichment processes beneath continental collisional belt. *Lithos* **2004**, *78*, 291–305. [[CrossRef](#)]
84. Richards, J.P.; Kerrich, R. Special Paper: Adakite-Like Rocks: Their Diverse Origins and Questionable Role in Metallogenesis. *Econ. Geol.* **2007**, *102*, 537–576. [[CrossRef](#)]
85. Wang, Q.; Xu, J.-F.; Jian, P.; Bao, Z.-W.; Zhao, Z.-H.; Li, C.-F.; Xiong, X.-L.; Ma, J.-L. Petrogenesis of Adakitic Porphyries in an Extensional Tectonic Setting, Dexing, South China: Implications for the Genesis of Porphyry Copper Mineralization. *J. Pet.* **2005**, *47*, 119–144. [[CrossRef](#)]
86. Liu, S.-A.; Li, S.; He, Y.; Huang, F. Geochemical contrasts between early Cretaceous ore-bearing and ore-barren high-Mg adakites in central-eastern China: Implications for petrogenesis and Cu–Au mineralization. *Geochim. Cosmochim. Acta* **2010**, *74*, 7160–7178. [[CrossRef](#)]
87. Long, X.; Yuan, C.; Sun, M.; Kröner, A.; Zhao, G.; Wilde, S.; Hu, A. Reworking of the Tarim Craton by underplating of mantle plume-derived magmas: Evidence from Neoproterozoic granitoids in the Kuluketage area, NW China. *Precambrian Res.* **2011**, *187*, 1–14. [[CrossRef](#)]
88. Wood, D.A.; Joron, J.-L.; Treuil, M. A re-appraisal of the use of trace elements to classify and discriminate between magma series erupted in different tectonic settings. *Earth Planet. Sci. Lett.* **1979**, *45*, 326–336. [[CrossRef](#)]
89. Brihuega, L.; Bougault, H.; Joron, J.L. Quantification of Nb, Ta, Ti and V anomalies in magmas associated with subduction zones: Petrogenetic implications. *Earth Planet. Sci. Lett.* **1984**, *68*, 297–308. [[CrossRef](#)]
90. Pearce, J.A. Geochemical fingerprinting of oceanic basalts with applications to ophiolite classification and the search for Archean oceanic crust. *Lithos* **2008**, *100*, 14–48. [[CrossRef](#)]
91. Xia, L.; Li, X. Basalt geochemistry as a diagnostic indicator of tectonic setting. *Gondwana Res.* **2018**, *65*, 43–67. [[CrossRef](#)]
92. He, Z.; Xu, X. Petrogenesis of the Late Yanshanian mantle-derived intrusions in southeastern China: Response to the geodynamics of paleo-Pacific plate subduction. *Chem. Geol.* **2012**, *328*, 208–221. [[CrossRef](#)]
93. Yang, C.; He, J.; Yang, F.; Wu, Y.; Li, Q. Petrogenesis and geodynamic significance of Kayinde gabbro in the Ashele Basin, Altay Orogenic Belt, Xinjiang, Northwest China: Constraints from geochronological and geochemical data. *Geol. J.* **2020**, *55*, 1849–1865. [[CrossRef](#)]
94. Wang, Z.; Li, Y.; Yang, G.; Zhang, Y.; Li, H.; Zhao, Y.; Lindagato, P. Geochronology, geochemistry, and petrogenesis of the Kezijiaer gabbros, southern Chinese Altai: Evidence for ridge subduction. *Geol. J.* **2020**, *55*, 2254–2268. [[CrossRef](#)]
95. Pearce, J.A.; Peate, D.W. Tectonic implications of the composition of volcanic arc magmas. *Annu. Rev. Earth Planet. Sci.* **1995**, *23*, 251–285. [[CrossRef](#)]
96. Whalen, J.B.; Currie, K.L.; Chappell, B.W. A-type granites: Geochemical characteristics, discrimination and petrogenesis. *Contrib. Mineral. Petrol.* **1987**, *95*, 407–419. [[CrossRef](#)]
97. King, P.L.; White, A.J.R.; Chappell, B.W.; Allen, C.M. Characterization and origin of aluminous A-type granites from the Lachlan Fold Belt, southeastern Australia. *J. Petrol.* **1997**, *38*, 371–391. [[CrossRef](#)]
98. Wu, F.-Y.; Sun, D.-Y.; Li, H.; Jahn, B.-M.; Wilde, S. A-type granites in northeastern China: Age and geochemical constraints on their petrogenesis. *Chem. Geol.* **2002**, *187*, 143–173. [[CrossRef](#)]
99. Li, X.H.; Li, Z.X.; Li, W.X.; Liu, Y.; Yuan, C.; Wei, G.; Qi, C. U–Pb zircon, geochemical and Sr–Nd–Hf isotopic constraints on age and origin of Jurassic I-and A-type granites from central Guangdong, SE China: A major igneous event in response to foundering of a subducted flat-slab? *Lithos* **2007**, *96*, 186–204. [[CrossRef](#)]
100. Barbarin, B. A review of the relationships between granitoid types, their origins and their geodynamic environments. *Lithos* **1999**, *46*, 605–626. [[CrossRef](#)]
101. Chappell, B. Aluminium saturation in I- and S-type granites and the characterization of fractionated haplogranites. *Lithos* **1999**, *46*, 535–551. [[CrossRef](#)]
102. Wyborn, D.; Turner, B.S.; Chappell, B.W. The Boggy Plain Supersuite: A distinctive belt of I-type igneous rocks of potential economic significance in the Lachlan Fold Belt. *Aust. J. Earth Sci.* **1987**, *34*, 21–43. [[CrossRef](#)]
103. Kemp, A.I.S.; Hawkesworth, C.J.; Foster, G.L.; Paterson, B.A.; Woodhead, J.D.; Hergt, J.M.; Gray, C.M.; Whitehouse, M.J. Magmatic and Crustal Differentiation History of Granitic Rocks from Hf–O Isotopes in Zircon. *Science* **2007**, *315*, 980–983. [[CrossRef](#)]
104. Chappel, B.W.; White, A. Two contrasting granite types. *Pac. Geol.* **1974**, *8*, 173–174.
105. Du, L.; Zhang, Y.; Huang, Z.; Li, X.-P.; Yuan, C.; Wu, B.; Long, X. Devonian to carboniferous tectonic evolution of the Kangguer Ocean in the Eastern Tianshan, NW China: Insights from three episodes of granitoids. *Lithos* **2019**, *350–351*, 105243. [[CrossRef](#)]
106. Frey, F.A.; Garcia, M.O.; Roden, M.F. Geochemical characteristics of Koolau Volcano: Implications of intershield geochemical differences among Hawaiian volcanoes. *Geochim. Cosmochim. Acta* **1994**, *58*, 1441–1462. [[CrossRef](#)]
107. Hofmann, A.W. Chemical differentiation of the Earth: The relationship between mantle, continental crust, and oceanic crust. *Earth Planet. Sci. Lett.* **1988**, *90*, 297–314. [[CrossRef](#)]

108. Xiao, W.-J.; Zhang, L.-C.; Qin, K.-Z.; Sun, S.; Li, J.-L. Paleozoic accretionary and collisional tectonics of the eastern Tianshan (China): Implications for the continental growth of central Asia. *Am. J. Sci.* **2004**, *304*, 370–395. [[CrossRef](#)]
109. Wang, Y.-H.; Zhang, F.-F. Petrogenesis of early Silurian intrusions in the Sanchakou area of Eastern Tianshan, Northwest China, and tectonic implications: Geochronological, geochemical, and Hf isotopic evidence. *Int. Geol. Rev.* **2016**, *58*, 1294–1310. [[CrossRef](#)]
110. Zhang, W.; Zhang, F.F.; Wang, Y.H.; Xue, C.J.; Wang, J.P.; Sun, M.; Wang, K. Origin of Paleozoic granitoids in the Yuhai Cu–Mo deposit, Eastern Tianshan, NW China and implications for regional metallogeny. *Ore Geol. Rev.* **2020**, *121*, 103465. [[CrossRef](#)]
111. Wood, D.A. The application of a Th–Hf–Ta diagram to problems of tectonomagmatic classification and to establishing the nature of crustal contamination of basaltic lavas of the British Tertiary Volcanic Province. *Earth Planet. Sci. Lett.* **1980**, *50*, 11–30. [[CrossRef](#)]
112. Du, L.; Zhu, H.; Yuan, C.; Zhang, Y.; Huang, Z.; Li, X.-P.; Long, X. Paleozoic crustal evolution and tectonic switching in the Northeastern Tianshan: Insights from zircon Hf isotopes of granitoids. *J. Geol. Soc.* **2020**, *178*. [[CrossRef](#)]
113. Pearce, J.A.; Harris, N.B.W.; Tindle, A.G. Trace Element Discrimination Diagrams for the Tectonic Interpretation of Granitic Rocks. *J. Pet.* **1984**, *25*, 956–983. [[CrossRef](#)]
114. Harris, N.B.W.; Pearce, J.A.; Tindle, A.G. Geochemical characteristics of collision-zone magmatism. In *Geological Society; Special Publications*; London, UK, 1986; Volume 19, pp. 67–81.
115. Zhang, Z.; Ding, H.; Dong, X.; Tian, Z. Partial melting of subduction zones. *Acta Petrol. Sin.* **2020**, *36*, 2589–2615.
116. Wang, Q.; Xu, J.F.; Zhao, Z.H.; Zi, F.; Tang, G.J.; Jia, X.H.; Jiang, Z.Q. Tectonic setting and associated rock suites of adakitic rocks. *Bull. Mineral. Petr. Geochem.* **2008**, *27*, 344–350.
117. Sajona, F.G.; Maury, R.C.; Bellon, H.; Cotten, J.; Defant, M.J.; Pubellier, M. Initiation of subduction and the generation of slab melts in western and eastern Mindanao, Philippines. *Geology* **1993**, *21*, 1007–1010. [[CrossRef](#)]
118. Tang, G.; Wang, Q.; Wyman, D.A.; Li, Z.-X.; Zhao, Z.-H.; Jia, X.-H.; Jiang, Z.-Q. Ridge subduction and crustal growth in the Central Asian Orogenic Belt: Evidence from Late Carboniferous adakites and high-Mg diorites in the western Junggar region, northern Xinjiang (west China). *Chem. Geol.* **2010**, *277*, 281–300. [[CrossRef](#)]
119. Gutscher, M.A.; Maury, R.; Eissen, J.P.; Bourdon, E. Can slab melting be caused by flat subduction? *Geology* **2000**, *28*, 535–538. [[CrossRef](#)]
120. Wang, Q.; Tang, G.; Hao, L.; Wyman, D.; Ma, L.; Dan, W.; Zhang, X.; Liu, J.; Huang, T.; Xu, C. Ridge subduction, magmatism, and metallogenesis. *Sci. China Earth Sci.* **2020**, *63*, 1499–1518. [[CrossRef](#)]
121. Cao, M.; Qin, K.; Li, J. Research progress on the flat subduction and its metallogenic effect, two cases analysis and some prospects. *Acta Petrol. Sin.* **2011**, *27*, 3727–3748.
122. Qiu, M.; Zhao, Y.; Xue, C.; Chen, J.; Ma, X.; Wang, L.; Yu, L.; You, Y. genesis of the Ni–Cu sulfide mineralization of the carboniferous Haibaotan intrusion, Eastern Tianshan, Central Asian Orogenic Belt. *Int. J. Earth Sci.* **2022**, *1*–26. [[CrossRef](#)]
123. Tang, G.-J.; Chung, S.-L.; Hawkesworth, C.J.; Cawood, P.; Wang, Q.; Wyman, D.A.; Xu, Y.-G.; Zhao, Z.-H. Short episodes of crust generation during protracted accretionary processes: Evidence from Central Asian Orogenic Belt, NW China. *Earth Planet. Sci. Lett.* **2017**, *464*, 142–154. [[CrossRef](#)]